

**A peculiarly long-duration gamma-ray burst from binary neutron star merger**JUN YANG,<sup>1,2</sup> BIN-BIN ZHANG,<sup>1,2</sup> SHUNKE AI,<sup>3,4</sup> ZI-KE LIU,<sup>1,2</sup> XIANGYU IVY WANG,<sup>1,2</sup> YE LI,<sup>5</sup> HOU-JUN LÜ,<sup>6</sup> AND BING ZHANG<sup>3,4</sup><sup>1</sup>*School of Astronomy and Space Science, Nanjing University, Nanjing 210093, China*<sup>2</sup>*Key Laboratory of Modern Astronomy and Astrophysics (Nanjing University), Ministry of Education, China*<sup>3</sup>*Nevada Center for Astrophysics, University of Nevada Las Vegas, NV 89154, USA*<sup>4</sup>*Department of Physics and Astronomy, University of Nevada Las Vegas, NV 89154, USA*<sup>5</sup>*Purple Mountain Observatory, Chinese Academy of Sciences, Nanjing 210023, China*<sup>6</sup>*Guangxi Key Laboratory for Relativistic Astrophysics, School of Physical Science and Technology, Guangxi University, Nanning 530004, China;***ABSTRACT**

Some recent findings have shown that the duration of gamma-ray burst (GRB), although crucially related to the GRB central engine time scale, is not determinative in inferring the GRB origins in terms of their progenitors. In this paper, we report a peculiarly long-duration gamma-ray burst, GRB 211211A, that is associated with a kilonova in optical and near-infrared bands and is therefore likely the result of a binary neutron star merger. The burst broadly resembles the properties of GRB 060614 but with a much higher brightness in its light curve and harder spectra in both the main and extended emission phases, making it difficult to be explained as a short GRB with soft extended emission. Such a genuinely long-duration GRB suggests that merger product is likely a magnetar, which powers up the burst through magnetic and rotation energy for at least  $\sim 70$  seconds.

**1. INTRODUCTION**

Over the last few decades, multi-wavelength and multi-messenger observations have established that Type-II gamma-ray bursts (GRBs) usually originate from the core collapse of massive stars and Type-I GRBs from the merger of compact binaries. The conclusive evidence for those two origins has been discovered through, e.g., the characteristic spectral lines of supernova (SN) in the optical afterglow of Type-II GRBs (Galama et al. 1998; Reeves et al. 2002; Hjorth et al. 2003), and the joint detection of GW170817, Type-I GRB 170817A, and kilonova (KN) AT2017gfo (Abbott et al. 2017; Goldstein et al. 2017; Zhang et al. 2018; Coulter et al. 2017; Pian et al. 2017). The diversity of GRB origins has been further expanded by the short GRB 200415A, which was confirmed to originate from a young magnetar giant flare (MGF) in the starburst galaxy NGC 253 (Yang et al. 2020; Roberts et al. 2021; Svinkin et al. 2021; Fermi-LAT Collaboration et al. 2021). Indeed, the MGF GRBs form the third track (Yang et al. 2020; Zhang et al. 2020) in the  $E_{p,z} - E_{\gamma,\text{iso}}$  diagram (a.k.a. Amati relation; Amati

et al. 2002) and, therefore, can be referred to as “Type-III” GRBs.

GRB classification has evolved into a multi-criteria task based on a range of criteria, such as burst duration, spectral behavior, total energy, supernova/kilonova association, and host galaxy type and offset, etc (Zhang et al. 2009a). Moreover, burst duration has become increasingly less significant compared to other factors, especially since recent evidence shows that bursts longer (shorter) than 2 seconds do not necessarily correspond to Type II (I) origins. Those outliers include, e.g., GRB 060614 (Gal-Yam et al. 2006; Fynbo et al. 2006; Della Valle et al. 2006; Gehrels et al. 2006; Zhang et al. 2007a; Yang et al. 2015), GRB 090426 (Antonelli et al. 2009; Levesque et al. 2010; Xin et al. 2011), GBR 211227A (Lü et al. 2022), and GRB 200826A (Zhang et al. 2021; Ahumada et al. 2021). Nevertheless, burst duration remains crucially linked to the central engine time scale of a GRB, and well-determined burst durations can be used to probe the physics underlying the GRB mechanism.

Recently, another outlier burst, GRB 211211A, was detected by multiple high-energy telescopes including *Fermi* (Fermi GBM Team 2021) and *Swift* (D’Ai et al. 2021). It shares a similar temporal profile with GRB

060614 but consists of a much more significant and erratic main emission and a spectrally harder tail. Thus, a soft extended emission cannot be attributed to the long duration of GRB 211211A, as had been the case in GRB 060614. Moreover, the optical counterpart is much fainter than an expected supernova, which further excludes its being a Type-II GRB.

In this *Letter*, we first perform a comprehensive analysis of the multi-wavelength data of GRB 211211A in §2, along with a comparison study between GRB 211211A and GRB 060614. By fitting the long-term multi-wavelength data with the theoretical afterglow and kilonova models, we confirm the existence of a kilonova component in §3. We further discussed the physical implications and the nature of the burst in §4, followed by a brief summary in §5.

## 2. DATA ANALYSIS

In this section, we present a comprehensive analysis of GRB 211211A focusing on its prompt emission, host galaxy and multi-wavelength afterglow. Considering the similarity between this burst and GRB 060614, we also compare some properties of the two bursts where applicable. Our analysis is summarized in Table 1 and detailed below.

### 2.1. Prompt Emission

GRB 211211A triggered the Gamma-ray Burst Monitor (GBM; Meegan et al. 2009) onboard *Fermi* at 2021 December 11 13:09:59 UTC (hereafter  $T_0$ ). We retrieved the time-tagged event dataset covering the time range of GRB 211211A from the *Fermi*/GBM public data archive<sup>1</sup>. Two sodium iodide (NaI) detectors, namely n2 and na, with the smallest viewing angles in respect to the GRB source direction, are selected for our analysis. Additionally, one bismuth germanium oxide (BGO) detector, b0, closest to the GRB direction, was also selected for spectral analysis. Since GRB 211211A is also detected by the Burst Alert Telescope (BAT; Barthelmy et al. 2005) onboard *Swift* (Gehrels et al. 2004), we also employ those BAT data in our analysis. *Swift*/BAT data are downloaded from *Swift* archive website<sup>2</sup>.

#### 2.1.1. Light Curve

Figure 1a and 1b shows the background-subtracted light curves observed by *Swift*/BAT and *Fermi*/GBM, respectively. The BAT light curve is obtained follow-

**Table 1.** Summary of the observed properties of GRB 211211A and GRB 060614.

	GRB 211211A	GRB 060614 <sup>a</sup>
<b>Main Emission:</b>		
Duration (s)	13	6
Averaged variability (ms)	16	...
Spectral lag (ms) <sup>b</sup>	$10^{+3}_{-4}$	$3 \pm 6$
Spectral index $\alpha$	$-1.00^{+0.00}_{-0.01}$	$-1.57^{+0.12}_{-0.14}$
Spectral index $\beta$	$-2.36^{+0.02}_{-0.02}$	...
Peak energy (keV)	$687.12^{+12.54}_{-11.05}$	$302^{+214}_{-85}$
Energy fluence (erg cm <sup>-2</sup> )	$3.77^{+0.01}_{-0.01} \times 10^{-4}$	$8.19^{+0.56}_{-2.52} \times 10^{-6}$
Isotropic energy (erg)	$5.30^{+0.01}_{-0.01} \times 10^{51}$	$3.18^{+0.22}_{-0.98} \times 10^{50}$
<b>Extended Emission:</b>		
Duration (s)	55	100
Averaged variability (ms)	48	...
Spectral lag (ms)	$5^{+5}_{-5}$	$3 \pm 9$
Spectral index $\alpha$	$-0.97^{+0.03}_{-0.04}$	$-2.13 \pm 0.05$
Spectral index $\beta$	$-2.02^{+0.01}_{-0.02}$	...
Peak energy (keV)	$82.02^{+3.77}_{-2.31}$	$\lesssim 20$
Energy fluence (erg cm <sup>-2</sup> )	$1.61^{+0.01}_{-0.01} \times 10^{-4}$	$3.27^{+0.17}_{-0.23} \times 10^{-5}$
Isotropic energy (erg)	$2.26^{+0.01}_{-0.01} \times 10^{51}$	$1.27^{+0.06}_{-0.09} \times 10^{51}$
<b>Whole Burst:</b>		
$T_{90}$ (s)	$43.18^{+0.06}_{-0.06}$	$102 \pm 5$
Spectral lag (ms)	$12 \pm 10$	...
$f_{\text{eff}}$ parameter	$1.24 \pm 0.07$	$2.26 \pm 0.23$
Spectral index $\alpha$	$-1.20^{+0.01}_{-0.01}$	...
Spectral index $\beta$	$-2.05^{+0.02}_{-0.02}$	...
Peak energy (keV)	$399.29^{+14.04}_{-16.06}$	$10 - 100$
Peak flux (erg cm <sup>-2</sup> s <sup>-1</sup> )	$1.38^{+0.02}_{-0.02} \times 10^{-4}$	$4.50^{+0.72}_{-1.53} \times 10^{-6}$
Total fluence (erg cm <sup>-2</sup> )	$(5.42 \pm 0.08) \times 10^{-4}$	$4.09^{+0.18}_{-0.34} \times 10^{-5}$
Peak luminosity (erg s <sup>-1</sup> )	$1.94^{+0.03}_{-0.03} \times 10^{51}$	$1.74^{+0.28}_{-0.59} \times 10^{50}$
Isotropic energy (erg)	$(7.61 \pm 0.11) \times 10^{51}$	$1.59^{+0.07}_{-0.13} \times 10^{51}$
<b>Host Galaxy:</b>		
Redshift	0.076	0.125
Half-light radius (kpc)	1.05	0.739
Offset (kpc)	9.48	$0.801 \pm 0.031$
Normalized offset	9.02	$1.086 \pm 0.042$
<b>Associations:</b>		
Kilonova	Yes	Yes
Supernova	No	No

NOTE—

a: The references for GRB 060614: Golenetskii et al. (2006); Della Valle et al. (2006); Amati et al. (2007); Yang et al. (2015); Blanchard et al. (2016); Li et al. (2016a).

b: The maximum spectral lag derived from *Fermi*/GBM data in the corresponding time interval.

ing the standard analysis threads<sup>3</sup> using the *HEASoft* tools (version 6.28). We first check the energy conversion of BAT event data using *bateconvert*. Next *batbinevt*, *bathotpix* and *batmaskwtevt* are utilized to generate the detector plane image, remove the hot pixels and apply mask-weighting, respectively. Then the BAT light curve is created with a bin size of 0.2 s and with

<sup>1</sup> <https://heasarc.gsfc.nasa.gov/FTP/fermi/data/gbm/daily/>

<sup>2</sup> <https://www.swift.ac.uk/archive/ql.php>

<sup>3</sup> <https://www.swift.ac.uk/analysis/bat/>

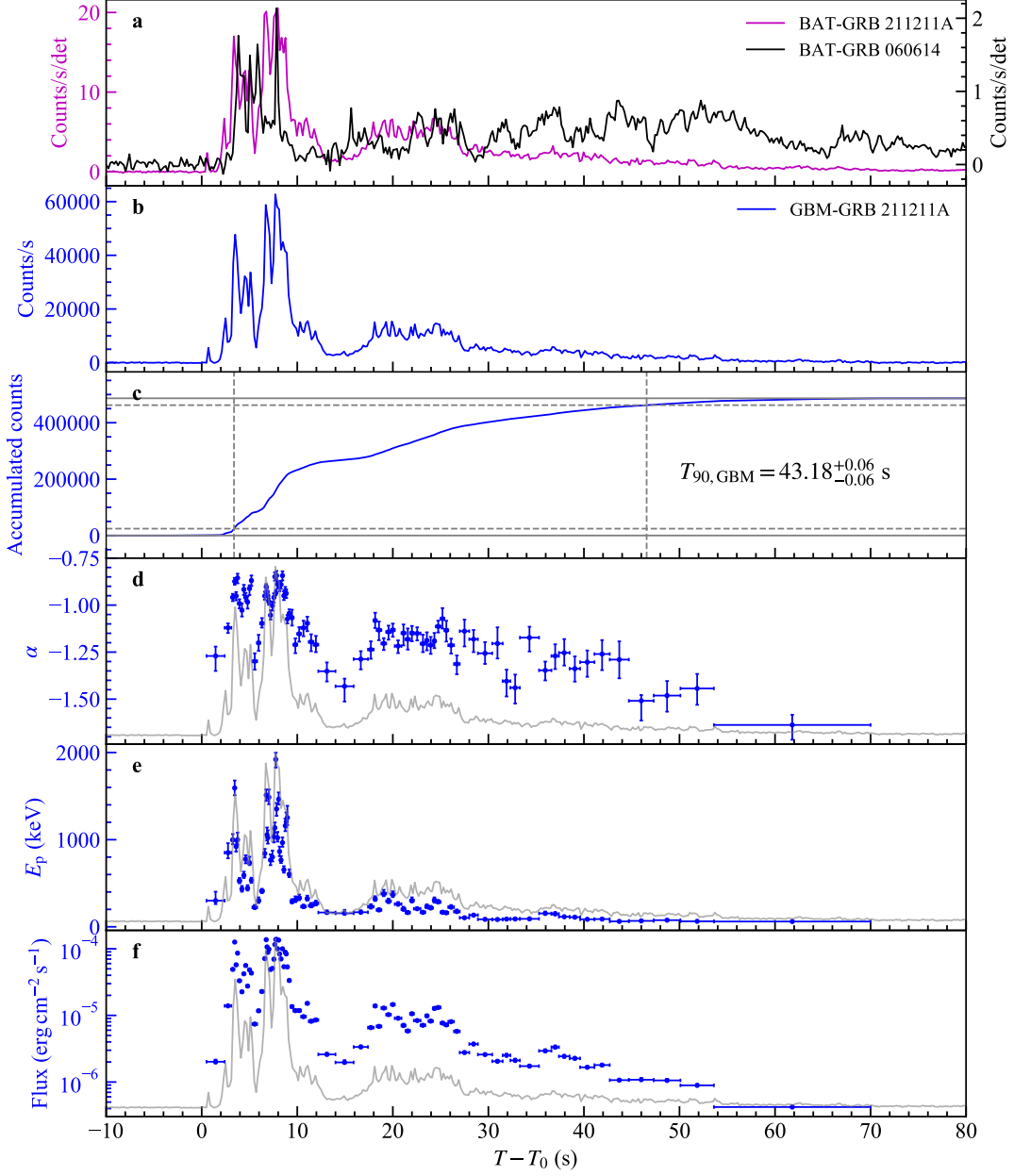


**Figure 1.** The temporal and spectral behaviors of GRB 211211A. **a**, The net light curves of GRB 211211A (purple) and GRB 060614 (black) obtained from *Swift*/BAT data. **b**, The net light curve of GRB 211211A obtained from *Fermi*/GBM data. **c**: The accumulated counts of the *Fermi*/GBM net light curve. The grey horizontal dashed (solid) lines are drawn at 5% (0%) and 95% (100%) of the total accumulated counts. The  $T_{90, \text{GBM}}$  interval is marked by the grey vertical dashed lines. **d**, **e** and **f** show the evolution of spectral index  $\alpha$ , peak energy  $E_p$  and energy flux. The *Fermi*/GBM net light curve (gray) is plotted in background as a reference.

the energy range of 15-350 keV using *batbinevt*. The  $T_{90, \text{BAT}}$  of GRB 211211A is determined by *battblocks* to be  $51.00 \pm 1.02$  s. The GBM light curve is derived by binning the photons with a bin size of 0.2 s in the energy range 10-1000 keV collected from the selected two NaI detectors (namely, n2 and na). The background level is

modeled by the baseline algorithm in *pybaseline*<sup>4</sup> package. The burst duration,  $T_{90, \text{GBM}}$ , determined by the time difference between the epochs when the total accumulated net photon counts within 10-1000 (50-300) keV

<sup>4</sup> <https://github.com/derb12/pybaselines>

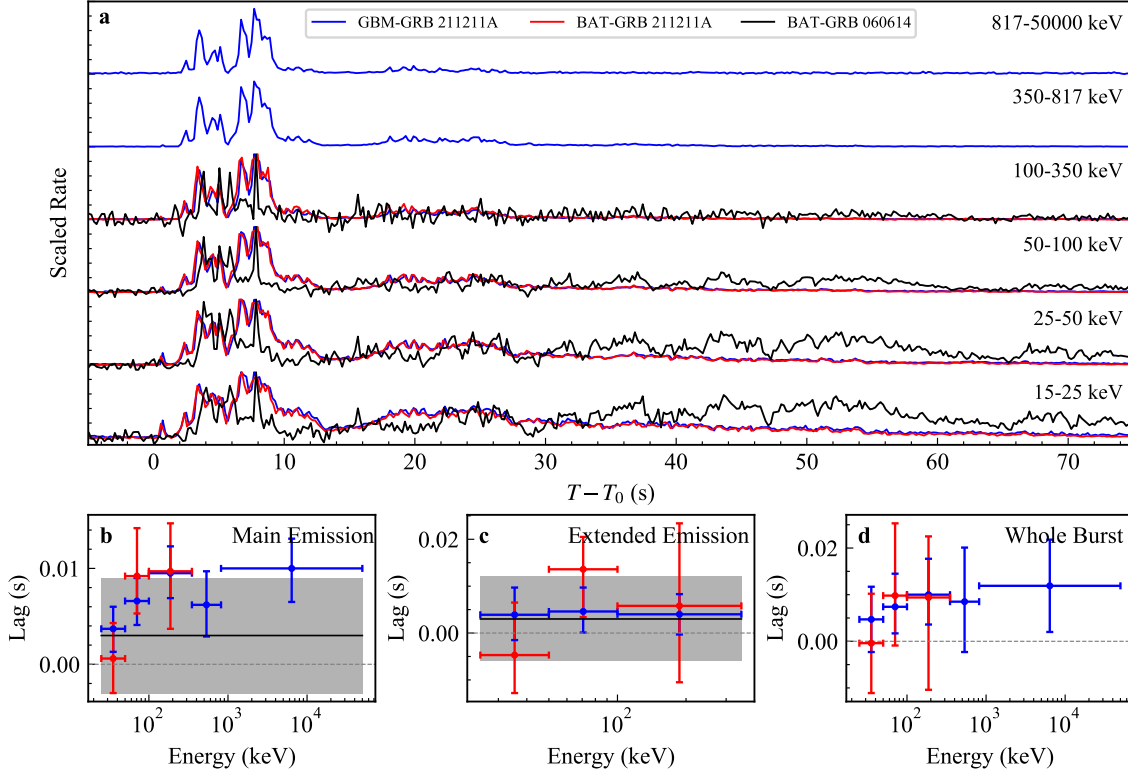


**Figure 2.** The multi-wavelength light curves of prompt emissions and spectral lags. **a**, The scaled multi-wavelength light curves obtained from *Fermi*/GBM (blue) and *Swift*/BAT (red) data for GRB 211211A, and *Swift*/BAT (black) data for GRB 060614. **b**, **c** and **d** show the spectral lags between each of the higher energy bands and the lowest energy band calculated for the main emission, extended emission, and whole burst of GRB 211211A. The lags in blue and red are derived from *Fermi*/GBM and *Swift*/BAT data, respectively. The horizontal black lines and grey shaded areas in **b**, and **c** show the spectral lags and their uncertainties of GRB 060614, respectively.

reaches the 5% level and the 95% level, is calculated to be  $43.18^{+0.06}_{-0.06}$  ( $36.58^{+0.02}_{-0.02}$ ) s (Figure 1c).

The light curves in Figure 1a and 1b exhibit two distinct phases, namely, main emission (ME) and extended emission (EE). The main emission is a sharply changing phase (lasts for approximately 13 seconds) that is characterized by several hard spikes. Following a relatively quiescent time of  $\sim 2$  s, the extended emission phase appears as a decaying tail extending to  $T_0 + 70$  s. The ME+EE feature was also observed in GRB 060614 (black line in Figure 1a). However, as discussed in §2.1.4, the spectra of both phases of GRB 211211A are much harder than those of GRB 060614. In addition, GRB 211211A exhibits a longer ME and a shorter EE in comparison with GRB 060614, as listed in Table 1.

Interestingly, the variability time scales of the ME and EE of GRB 211211A are different. We apply the Bayesian block method (Scargle et al. 2013) onto the un-binned event data of the two phases and take half of the averaged block size as the mean variability time scale (e.g., Vianello et al. 2018). Our results yield  $\tau_{\text{var}} \sim 16$  ms for the ME phase and  $\tau_{\text{var}} \sim 48$  ms for the EE phase,

suggesting a much smoother time profile in the latter phase.

### 2.1.2. Spectral Lags

The  $\gamma$ -ray light curves can be further studied in a multi-band manner by extracting them separately within several energy ranges from the event data. In Figure 2a, we plot such multi-band light curves for both GRB 211211A and GRB 060614. The temporal profiles of both bursts appear not to evolve with energy. Contrary to GRB 060614, there is significant emission above 350 keV during the main emission phase of GRB 211211A, thanks to the broad energy coverage of *Fermi*/GBM detectors. We also note that the extended emission of GRB 060614 is dominated by photons softer than 50 keV.

The time-dependent photon behaviors can be further studied through spectral lags. Spectral lag refers to the systematic time delay of the soft-band light curve relative to the hard-band light curve, a phenomenon typically observed in GRB light curves. Type-II GRBs are often associated with significant spectral lags, whereas

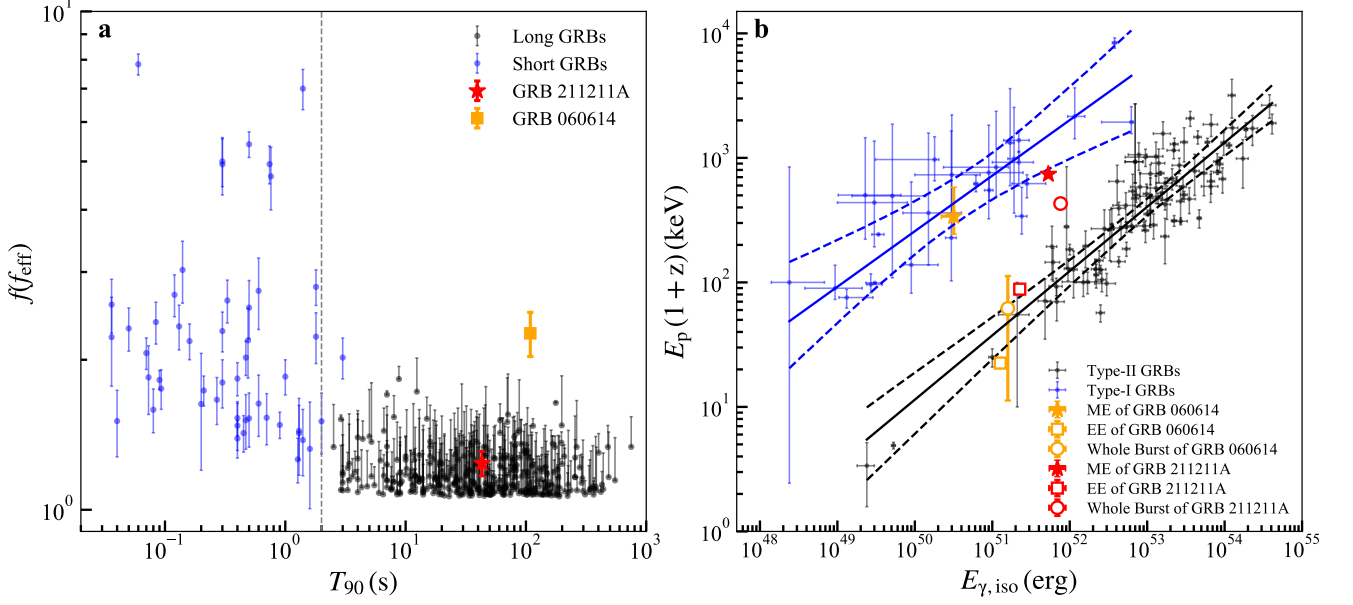


**Figure 3.** **a**, The  $f(f_{\text{eff}})$  and  $T_{90}$  diagram. Long and short GRBs are presented by black and blue circles, respectively. The grey vertical line is the division line at 2 s. GRB 211211A and GRB 060614 are highlighted by the red star and cyan square, respectively. **b**, The  $E_{p,z}$  and  $E_{\text{iso}}$  correlation diagram. The best-fit correlations (solid lines) and corresponding  $3\sigma$  confidence bands (dashed lines) are presented for Type-I (blue), Type-II (black) GRBs population, respectively. The main emission (ME), extended emission (EE), and whole burst for GRB 211211A (red) and GRB 060614 (purple) are highlighted by stars, squares, and circles, respectively.

Type-I GRBs tend to have a zero delay or even a negative lags (Yi et al. 2006; Bernardini et al. 2015).

We utilize the discrete cross-correlation function (DCCF; e.g., Norris et al. 2000; Ukwatta et al. 2010; Zhang et al. 2012) to measure the cross-correlation between the light curves of the softest band and each harder band in Figure 2a at different time delays. The DCCF values for different delays are fitted with a 3-order polynomial function to determine the spectral lag, which is defined as the time delay corresponding to the maximum cross-correlation. We calculate spectral lags separately for the main emission phase ( $T_0 + [-0.5, 14.0]$  s; Figure 2b), extended emission phase ( $T_0 + [14.0, 70.0]$  s; Figure 2c) and whole burst ( $T_0 + [-0.5, 70.0]$  s; Figure 2d). Figure 2b-d show that the spectral lags derived from data of GBM and BAT are in good agreement with each other, although the former one has smaller uncertainties. As a comparison, we obtain the lags of GRB 060614 from Gehrels et al. (2006) and also display them in Figure 2. According to Figure 2b-d, both GRBs exhibit tiny lags, a characteristic typically associated with Type-I GRBs (Yi et al. 2006; Bernardini et al. 2015; Shao et al. 2017).

### 2.1.3. Amplitude Parameter

The amplitude parameter,  $f$ , is defined as  $f = F_p/F_b$ , where  $F_p$  and  $F_b$  stand for the peak flux and background flux at the same epoch, respectively. In order

to distinguish intrinsically short Type-I GRBs from disguised short-duration GRBs due to the tip-of-iceberg effect, an effective amplitude parameter,  $f_{\text{eff}}$ , for long-duration GRBs, can be defined as  $f_{\text{eff}} = F_{p'}/F_b$ , which is the  $f$  value of “pseudo GRBs” whose flux is re-scaled from the initial flux so that  $T_{90}$  above the background flux is shorter than 2 s (Lü et al. 2014). A long-duration GRB with a smaller  $f_{\text{eff}}$  is more unlikely subject to the tip-of-iceberg effect (Lü et al. 2014; Zhang et al. 2021).

Following the calculation procedure presented in (Lü et al. 2014), we obtain the effective amplitude as  $f_{\text{eff}} = 1.24 \pm 0.07$  for GRB 211211A. Such a small  $f_{\text{eff}}$  places GRB 211211A to be consistent with the long-duration GRBs in the  $f(f_{\text{eff}}) - T_{90}$  diagram (Figure 3a), suggesting that its long duration is not subject to the tip-of-iceberg effect thus confirming the long-duration nature of the burst. On the contrary, the value of  $f_{\text{eff}}$  of GRB 060614, obtained from Li et al. (2016a), is significantly higher than those of other long-duration GRBs (Figure 3a), supporting that it is an intrinsically short-duration Type-I GRB.

### 2.1.4. Spectral Fitting

We perform detailed time-resolved and time-integrated spectral fitting using the GBM data from detectors n2, na and b0. According to the criterion

**Table 2.** Spectral fitting results and corresponding energy flux in each time interval of GRB 211211A.

t1 (s)	t2 (s)	$\alpha$ ( $\beta$ )	$E_p$ (keV)	flux (erg cm <sup>-2</sup> s <sup>-1</sup> )	pgstat/dof	t1 (s)	t2 (s)	$\alpha$	$E_p$ (keV)	flux (erg cm <sup>-2</sup> s <sup>-1</sup> )	pgstat/dof
0.5	13.0	$-1.06^{+0.00}_{-0.01}$ ( $-2.36^{+0.02}_{-0.02}$ )	$687.12^{+12.54}_{-11.05}$	$3.02^{+0.01}_{-0.01} \times 10^{-5}$	2399.59/361	10.9	11.2	$-1.10^{+0.04}_{-0.04}$	$323.93^{+33.24}_{-22.02}$	$1.52^{+0.06}_{-0.04} \times 10^{-5}$	332.01/362
15.0	70.0	$-0.97^{+0.03}_{-0.04}$ ( $-2.02^{+0.01}_{-0.02}$ )	$82.02^{+3.77}_{-2.31}$	$2.92^{+0.01}_{-0.02} \times 10^{-6}$	883.32/361	11.2	11.7	$-1.20^{+0.04}_{-0.05}$	$242.80^{+30.89}_{-20.39}$	$8.16^{+0.35}_{-0.30} \times 10^{-6}$	317.85/362
0.5	70.0	$-1.20^{+0.01}_{-0.01}$ ( $-2.05^{+0.02}_{-0.02}$ )	$399.29^{+14.04}_{-16.06}$	$7.24^{+0.04}_{-0.03} \times 10^{-6}$	2648.05/361	11.7	12.2	$-1.21^{+0.05}_{-0.04}$	$269.36^{+30.73}_{-24.50}$	$8.54^{+0.33}_{-0.31} \times 10^{-6}$	297.89/362
0.5	2.4	$-1.27^{+0.05}_{-0.08}$	$300.28^{+102.90}_{-39.30}$	$2.01^{+0.16}_{-0.11} \times 10^{-6}$	204.38/362	12.2	14.0	$-1.35^{+0.05}_{-0.05}$	$164.27^{+24.50}_{-13.57}$	$2.60^{+0.14}_{-0.10} \times 10^{-6}$	291.13/362
2.4	3.1	$-1.12^{+0.02}_{-0.03}$	$851.36^{+108.25}_{-65.45}$	$1.39^{+0.02}_{-0.02} \times 10^{-5}$	303.82/362	14.0	15.9	$-1.43^{+0.04}_{-0.08}$	$155.11^{+40.16}_{-12.41}$	$1.97^{+0.16}_{-0.07} \times 10^{-6}$	259.65/362
3.1	3.4	$-0.96^{+0.02}_{-0.02}$	$997.68^{+66.71}_{-49.36}$	$4.91^{+0.07}_{-0.06} \times 10^{-5}$	393.99/362	15.9	17.4	$-1.29^{+0.04}_{-0.05}$	$167.36^{+22.09}_{-12.22}$	$3.36^{+0.17}_{-0.11} \times 10^{-6}$	336.08/362
3.4	3.5	$-0.87^{+0.02}_{-0.02}$	$1593.61^{+85.76}_{-84.14}$	$1.26^{+0.02}_{-0.02} \times 10^{-4}$	440.78/362	17.4	18.0	$-1.24^{+0.04}_{-0.05}$	$230.52^{+28.83}_{-21.38}$	$6.56^{+0.29}_{-0.25} \times 10^{-6}$	289.01/362
3.5	3.7	$-0.95^{+0.02}_{-0.02}$	$923.10^{+60.79}_{-60.05}$	$5.74^{+0.07}_{-0.10} \times 10^{-5}$	377.34/362	18.0	18.3	$-1.08^{+0.04}_{-0.04}$	$319.02^{+32.25}_{-22.42}$	$1.39^{+0.05}_{-0.04} \times 10^{-5}$	301.40/362
3.7	3.8	$-0.86^{+0.02}_{-0.03}$	$999.20^{+82.19}_{-56.48}$	$8.60^{+0.16}_{-0.15} \times 10^{-5}$	379.22/362	18.3	18.8	$-1.13^{+0.05}_{-0.05}$	$193.54^{+18.44}_{-13.81}$	$6.85^{+0.30}_{-0.23} \times 10^{-6}$	285.09/362
3.8	4.1	$-0.99^{+0.02}_{-0.03}$	$527.97^{+32.56}_{-27.88}$	$3.31^{+0.05}_{-0.07} \times 10^{-5}$	402.86/362	18.8	19.3	$-1.20^{+0.03}_{-0.03}$	$380.68^{+43.85}_{-28.88}$	$1.29^{+0.04}_{-0.04} \times 10^{-5}$	365.17/362
4.1	4.315	$-1.03^{+0.04}_{-0.03}$	$433.84^{+35.03}_{-30.85}$	$2.26^{+0.06}_{-0.06} \times 10^{-5}$	323.71/362	19.3	19.8	$-1.14^{+0.03}_{-0.04}$	$294.28^{+30.01}_{-22.17}$	$1.03^{+0.03}_{-0.04} \times 10^{-5}$	363.09/362
4.315	4.5	$-0.92^{+0.02}_{-0.03}$	$590.83^{+41.70}_{-30.63}$	$4.21^{+0.08}_{-0.10} \times 10^{-5}$	337.54/362	19.8	20.2	$-1.13^{+0.04}_{-0.04}$	$370.66^{+36.82}_{-29.56}$	$1.46^{+0.04}_{-0.04} \times 10^{-5}$	366.96/362
4.5	4.7	$-0.96^{+0.02}_{-0.02}$	$775.60^{+45.38}_{-46.79}$	$5.61^{+0.09}_{-0.09} \times 10^{-5}$	386.44/362	20.2	20.9	$-1.22^{+0.03}_{-0.04}$	$260.30^{+24.57}_{-16.51}$	$9.06^{+0.31}_{-0.22} \times 10^{-6}$	303.95/362
4.7	4.9	$-0.98^{+0.03}_{-0.04}$	$442.31^{+35.64}_{-25.49}$	$2.75^{+0.07}_{-0.07} \times 10^{-5}$	336.71/362	20.9	21.33	$-1.15^{+0.05}_{-0.07}$	$201.57^{+28.52}_{-13.61}$	$7.05^{+0.42}_{-0.24} \times 10^{-6}$	296.20/362
4.9	5.1	$-0.91^{+0.02}_{-0.04}$	$734.93^{+70.65}_{-26.50}$	$4.83^{+0.09}_{-0.08} \times 10^{-5}$	365.44/362	21.33	21.8	$-1.18^{+0.06}_{-0.05}$	$163.45^{+15.62}_{-13.18}$	$5.84^{+0.26}_{-0.24} \times 10^{-6}$	312.70/362
5.1	5.3	$-0.87^{+0.03}_{-0.03}$	$534.13^{+29.37}_{-28.80}$	$4.32^{+0.06}_{-0.10} \times 10^{-5}$	323.32/362	21.8	22.2	$-1.15^{+0.04}_{-0.04}$	$302.32^{+35.71}_{-23.38}$	$1.06^{+0.04}_{-0.03} \times 10^{-5}$	334.77/362
5.3	5.8	$-1.30^{+0.04}_{-0.04}$	$223.43^{+28.63}_{-18.90}$	$7.40^{+0.32}_{-0.27} \times 10^{-6}$	326.06/362	22.2	22.9	$-1.15^{+0.04}_{-0.04}$	$207.28^{+14.66}_{-11.76}$	$8.36^{+0.25}_{-0.23} \times 10^{-6}$	355.29/362
5.8	6.105	$-1.20^{+0.04}_{-0.04}$	$300.81^{+36.98}_{-27.10}$	$1.17^{+0.05}_{-0.04} \times 10^{-5}$	326.81/362	22.9	23.4	$-1.21^{+0.05}_{-0.04}$	$166.71^{+13.50}_{-12.13}$	$7.11^{+0.27}_{-0.24} \times 10^{-6}$	312.39/362
6.105	6.5	$-1.10^{+0.03}_{-0.02}$	$411.42^{+24.90}_{-25.05}$	$2.28^{+0.05}_{-0.05} \times 10^{-5}$	363.45/362	23.4	23.73	$-1.19^{+0.04}_{-0.05}$	$231.67^{+26.34}_{-19.66}$	$9.85^{+0.42}_{-0.24} \times 10^{-6}$	298.87/362
6.5	6.7	$-0.95^{+0.02}_{-0.02}$	$841.66^{+52.42}_{-46.34}$	$7.13^{+0.11}_{-0.09} \times 10^{-5}$	458.43/362	23.73	24.2	$-1.21^{+0.04}_{-0.05}$	$217.07^{+23.57}_{-16.81}$	$8.22^{+0.36}_{-0.25} \times 10^{-6}$	322.31/362
6.7	6.8	$-0.90^{+0.01}_{-0.02}$	$1511.62^{+64.59}_{-67.08}$	$1.37^{+0.02}_{-0.02} \times 10^{-4}$	469.41/362	24.2	24.5	$-1.19^{+0.04}_{-0.04}$	$305.11^{+32.62}_{-27.42}$	$1.27^{+0.04}_{-0.04} \times 10^{-5}$	291.18/362
6.8	6.875	$-0.93^{+0.02}_{-0.03}$	$1055.48^{+84.01}_{-65.73}$	$1.07^{+0.02}_{-0.02} \times 10^{-4}$	396.71/362	24.5	25.0	$-1.11^{+0.03}_{-0.03}$	$285.57^{+23.02}_{-15.43}$	$1.31^{+0.03}_{-0.03} \times 10^{-5}$	337.06/362
6.875	6.965	$-0.95^{+0.03}_{-0.03}$	$1021.65^{+86.56}_{-67.18}$	$8.84^{+0.17}_{-0.16} \times 10^{-5}$	362.51/362	25.0	25.4	$-1.07^{+0.06}_{-0.05}$	$167.47^{+13.42}_{-11.06}$	$7.66^{+0.30}_{-0.27} \times 10^{-6}$	295.48/362
6.965	7.1	$-0.98^{+0.02}_{-0.02}$	$1486.83^{+88.95}_{-80.09}$	$9.83^{+0.17}_{-0.12} \times 10^{-5}$	502.24/362	25.4	25.8	$-1.13^{+0.05}_{-0.05}$	$160.52^{+15.32}_{-10.63}$	$7.21^{+0.32}_{-0.22} \times 10^{-6}$	285.70/362
7.1	7.3	$-1.05^{+0.03}_{-0.02}$	$765.90^{+65.07}_{-58.08}$	$4.89^{+0.08}_{-0.08} \times 10^{-5}$	465.77/362	25.8	26.4	$-1.21^{+0.04}_{-0.04}$	$225.74^{+24.26}_{-15.02}$	$8.05^{+0.34}_{-0.22} \times 10^{-6}$	304.57/362
7.3	7.5	$-1.00^{+0.02}_{-0.03}$	$800.34^{+74.96}_{-49.51}$	$5.08^{+0.09}_{-0.07} \times 10^{-5}$	406.72/362	26.4	27.0	$-1.31^{+0.05}_{-0.05}$	$174.89^{+23.65}_{-14.41}$	$5.76^{+0.30}_{-0.20} \times 10^{-6}$	279.77/362
7.5	7.61	$-0.96^{+0.02}_{-0.03}$	$1035.85^{+83.93}_{-67.52}$	$6.98^{+0.11}_{-0.17} \times 10^{-5}$	431.29/362	27.0	28.0	$-1.14^{+0.08}_{-0.08}$	$103.68^{+5.81}_{-5.81}$	$2.77^{+0.12}_{-0.09} \times 10^{-6}$	268.42/362
7.61	7.7	$-0.85^{+0.02}_{-0.02}$	$1136.77^{+61.38}_{-59.81}$	$1.16^{+0.02}_{-0.02} \times 10^{-4}$	487.18/362	28.0	28.9	$-1.18^{+0.05}_{-0.07}$	$133.94^{+13.82}_{-8.03}$	$3.71^{+0.17}_{-0.11} \times 10^{-6}$	293.07/362
7.7	7.8	$-0.94^{+0.02}_{-0.01}$	$1920.82^{+77.55}_{-93.80}$	$1.38^{+0.02}_{-0.02} \times 10^{-4}$	484.62/362	28.9	30.4	$-1.26^{+0.06}_{-0.06}$	$85.92^{+5.23}_{-4.21}$	$2.58^{+0.10}_{-0.07} \times 10^{-6}$	267.26/362
7.8	7.87	$-0.84^{+0.02}_{-0.02}$	$1352.45^{+69.46}_{-78.98}$	$1.38^{+0.03}_{-0.02} \times 10^{-4}$	420.36/362	30.4	31.5	$-1.20^{+0.09}_{-0.08}$	$83.63^{+6.99}_{-5.42}$	$2.05^{+0.09}_{-0.07} \times 10^{-6}$	280.33/362
7.87	8.0	$-0.89^{+0.02}_{-0.02}$	$1021.56^{+67.01}_{-43.37}$	$1.00^{+0.01}_{-0.01} \times 10^{-4}$	371.07/362	31.5	32.305	$-1.40^{+0.06}_{-0.08}$	$88.89^{+9.85}_{-6.83}$	$2.51^{+0.13}_{-0.09} \times 10^{-6}$	254.40/362
8.0	8.1	$-0.89^{+0.02}_{-0.02}$	$1464.06^{+78.29}_{-60.24}$	$1.35^{+0.02}_{-0.02} \times 10^{-4}$	451.51/362	32.305	33.3	$-1.44^{+0.07}_{-0.08}$	$90.07^{+12.23}_{-6.59}$	$2.11^{+0.13}_{-0.08} \times 10^{-6}$	245.51/362
8.1	8.2	$-0.90^{+0.03}_{-0.03}$	$864.65^{+56.17}_{-53.23}$	$8.36^{+0.14}_{-0.16} \times 10^{-5}$	386.92/362	33.3	35.3	$-1.17^{+0.06}_{-0.07}$	$91.42^{+7.10}_{-4.28}$	$1.73^{+0.07}_{-0.05} \times 10^{-6}$	255.59/362
8.2	8.4	$-0.89^{+0.02}_{-0.02}$	$766.17^{+45.27}_{-34.08}$	$7.05^{+0.09}_{-0.11} \times 10^{-5}$	453.50/362	35.3	36.6	$-1.35^{+0.05}_{-0.05}$	$153.81^{+21.30}_{-12.39}$	$2.93^{+0.15}_{-0.10} \times 10^{-6}$	298.30/362
8.4	8.5	$-0.84^{+0.02}_{-0.03}$	$965.77^{+60.49}_{-47.29}$	$9.99^{+0.16}_{-0.18} \times 10^{-5}$	354.00/362	36.6	37.38	$-1.27^{+0.06}_{-0.07}$	$147.73^{+21.94}_{-12.10}$	$3.33^{+0.20}_{-0.13} \times 10^{-6}$	272.55/362
8.5	8.7	$-0.95^{+0.02}_{-0.02}$	$654.45^{+41.73}_{-33.44}$	$5.38^{+0.09}_{-0.09} \times 10^{-5}$	402.11/362	37.38	38.5	$-1.25^{+0.07}_{-0.07}$	$115.34^{+12.35}_{-13.44}$	$2.43^{+0.11}_{-0.11} \times 10^{-6}$	241.96/362
8.7	8.795	$-0.92^{+0.02}_{-0.02}$	$1159.41^{+83.59}_{-61.61}$	$8.85^{+0.16}_{-0.16} \times 10^{-5}$	369.54/362	38.5	39.6	$-1.34^{+0.07}_{-0.07}$	$110.22^{+13.61}_{-7.54}$	$2.26^{+0.12}_{-0.08} \times 10^{-6}$	254.22/362
8.795	8.9	$-0.94^{+0.02}_{-0.02}$	$1204.84^{+109.10}_{-63.07}$	$8.37^{+0.14}_{-0.15} \times 10^{-5}$	375.64/362	39.6	41.1	$-1.30^{+0.06}_{-0.08}$	$86.35^{+7.40}_{-5.25}$	$1.66^{+0.07}_{-0.06} \times 10^{-6}$	256.25/362
8.9	9.03	$-1.07^{+0.02}_{-0.02}$	$1252.16^{+136.70}_{-83.84}$	$5.35^{+0.10}_{-0.11} \times 10^{-5}$	433.73/362	41.1	42.7	$-1.26^{+0.07}_{-0.09}$	$88.79^{+8.89}_{-5.90}$	$1.80^{+0.09}_{-0.06} \times 10^{-6}$	240.01/362
9.03	9.3	$-1.04^{+0.02}_{-0.03}$	$603.57^{+55.18}_{-33.19}$	$3.35^{+0.06}_{-0.06} \times 10^{-5}$	300.74/362	42.7	44.7	$-1.29^{+0.10}_{-0.10}$	$62.39^{+4.46}_{-4.06}$	$1.07^{+0.04}_{-0.04} \times 10^{-6}$	203.05/362
9.3	9.6	$-1.07^{+0.04}_{-0.04}$	$291.42^{+26.18}_{-23.20}$	$1.35^{+0.05}_{-0.05} \times 10^{-5}$	344.43/362	44.7	47.3	$-1.51^{+0.03}_{-0.11}$	$68.07^{+9.86}_{-2.83}$	$1.08^{+0.07}_{-0.02} \times 10^{-6}$	234.63/362
9.6	10.0	$-1.21^{+0.03}_{-0.05}$	$307.45^{+42.04}_{-24.02}$	$1.18^{+0.05}_{-0.04} \times 10^{-5}$	312.69/362	47.3	50.1	$-1.48^{+0.08}_{-0.09}$	$76.23^{+8.92}_{-6.03}$	$1.06^{+0.06}_{-0.04} \times 10^{-6}$	208.91/362
10.0	10.4	$-1.15^{+0.04}_{-0.04}$	$330.96^{+39.02}_{-25.30}$	$1.18^{+0.05}_{-0.03} \times 10^{-5}$	330.12/362	50.1	53.6	$-1.44^{+0.08}_{-0.09}$	$63.13^{+5.44}_{-3.88}$	$8.91^{+0.40}_{-0.33} \times 10^{-7}$	247.34/362
10.4	10.9	$-1.12^{+0.04}_{-0.04}$	$232.23^{+22.09}_{-16.54}$	$9.57^{+0.40}_{-0.30} \times 10^{-6}$	346.45/362	53.6	70.0	$-1.64^{+0.05}_{-0.08}$	$60.76^{+7.38}_{-4.57}$	$4.21^{+0.24}_{-0.15} \times 10^{-7}$	218.64/362

that the average number of net photons per energy channel is not less than 20 (Zhang et al. 2018), the time interval from  $T_0 + 0.5$  to  $T_0 + 70$  s is divided into 85 time slices for time-resolved spectral fitting. We also bracket three time slices covering the main emission phase, extended emission phase, and whole burst, which are used for time-integrated spectral fitting. For each time slice, the source and background spectra are acquired by summing the total photons and background photons for each energy channel, where the background

photon number is derived by applying the baseline algorithm to each energy channel. The detector response matrix is generated by *gbm.drm\_gen* package (Burgess et al. 2018; Berlato et al. 2019). Then we use a self-developed software package, *MySpecFit*, to perform the spectral fitting. *MySpecFit* employs the nested sampler *Multinest* (Feroz & Hobson 2008; Feroz et al. 2009; Buchner et al. 2014; Feroz et al. 2019) as the fitting engine, and PGSTAT (Arnaud 1996) as the statistic to estimate uncertainties of the best-fit parameters. The

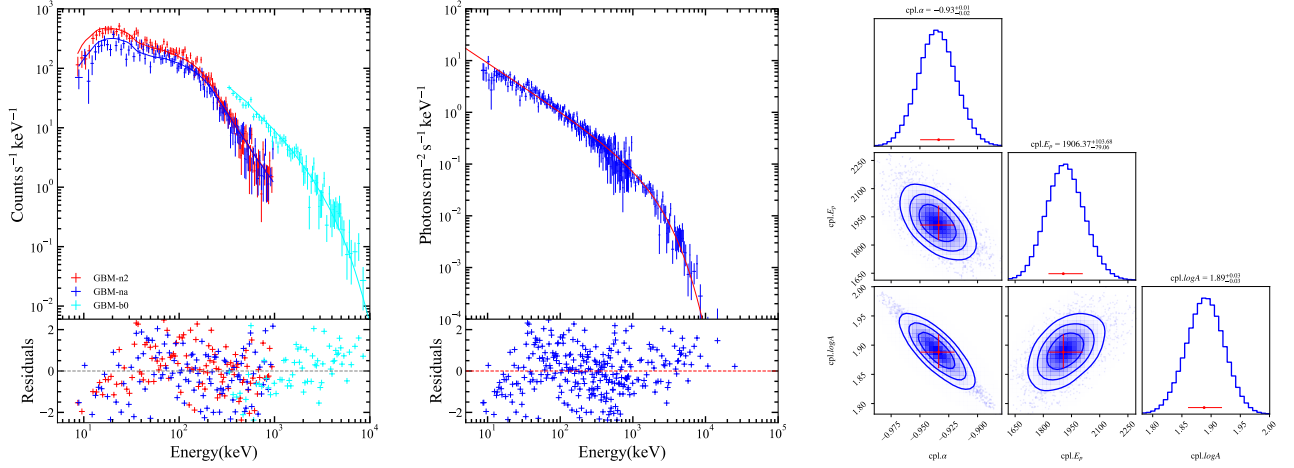


**Figure 4.** An example showing the spectral fitting using the CPL model for the time-resolved spectra measured from  $T_0 + 7.7$  to  $T_0 + 7.8$  s. *Left*, Observed and modeled photon count spectra. *Middle*, De-convolved (blue error bars) and modeled (red line) photon number spectrum. *Right*: Corner diagram for the best-fit parameters of the CPL model, in which the error bars represent the  $1\sigma$  uncertainties.

cutoff power law (CPL) and band function (Band; Band et al. 1993) are adopted to fit time-resolved spectra and time-integrated spectra, respectively. The CPL & Band models can be expressed as

$$N(E) = AE^\alpha \exp(-E/E_c) \quad (1)$$

and

$$N(E) = \begin{cases} A \left( \frac{E}{100 \text{ keV}} \right)^\alpha \exp\left(-\frac{E}{E_c}\right), & E < (\alpha - \beta)E_c \\ A \left[ \frac{(\alpha - \beta)E_c}{100 \text{ keV}} \right]^{\alpha - \beta} \exp(\beta - \alpha) \left( \frac{E}{100 \text{ keV}} \right)^\beta, & E \geq (\alpha - \beta)E_c \end{cases} \quad (2)$$

respectively, where  $\alpha$  and  $\beta$  are low-energy and high-energy photon spectral indices. The peak energy  $E_p$  is related to the cut-off energy,  $E_c$ , through  $E_p = (2 + \alpha)E_c$ .

Table 2 shows the spectral fitting results as well as the corresponding energy fluxes between 10 and 1000 keV. For the whole burst within 0.5 – 70.0 s, the Band model provides an acceptable fit with  $\alpha = -1.20^{+0.01}_{-0.01}$ ,  $\beta = -2.05^{+0.02}_{-0.02}$  and  $E_p = 399.29^{+14.04}_{-16.06}$  keV. The time-integrated spectrum of the main emission phase measured from  $T_0 + 0.5$  to  $T_0 + 13.0$  s is best fitted by the Band model with  $\alpha = -1.00^{+0.00}_{-0.01}$ ,  $\beta = -2.36^{+0.02}_{-0.02}$  and  $E_p = 687.12^{+12.54}_{-11.05}$  keV. The extended emission phase between  $T_0 + 15.0$  and  $T_0 + 70.0$  is best fitted by the Band model with  $\alpha = -0.97^{+0.03}_{-0.04}$ ,  $\beta = -2.02^{+0.01}_{-0.02}$  and  $E_p = 82.02^{+3.77}_{-2.31}$  keV. Comparatively, those spectra in both phases are much harder than those in the ME and EE phases of GRB 060614 (Table 1; Gehrels et al. 2006; Golenetskii et al. 2006; Amati et al. 2007).

The time-resolved spectra can be acceptably fitted by the CPL model. An example, including the photon

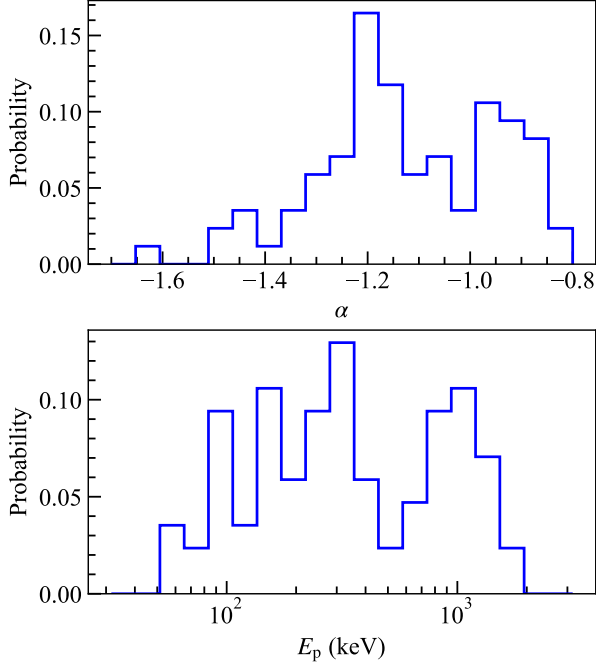
count spectra, photon number spectra, and corner diagram for the best-fit parameters, is shown in Figure 4. As shown in Figure 5,  $E_p$  distributes in a wide range between 60 keV and 1.9 MeV. The hardest time-resolved spectrum measured from  $T_0 + 7.7$  to  $T_0 + 7.8$  s is characterized by  $\alpha = -0.93^{+0.02}_{-0.01}$  and  $E_p = 1906.37^{+103.68}_{-79.06}$  keV, corresponding to the 0.1-s peak flux of  $1.38^{+0.02}_{-0.02} \times 10^{-4}$  erg cm $^{-2}$  s $^{-1}$ . Summing up all the fluence values derived from time-resolved spectral fitting, we further calculate the total fluence to be  $(5.42 \pm 0.08) \times 10^{-4}$  erg cm $^{-2}$ .

The evolution of  $\alpha$ ,  $E_p$  and energy flux of each time slice collected from the time-resolved spectral fits are over-plotted in the three bottom panels of Figure 1d-f. Both  $\alpha$  and  $E_p$  exhibit the same “flux-tracking” evolution patterns simultaneously (“double-tracking”; Lu et al. 2012; Li et al. 2019) across the entire burst. The tracking behaviors can be further verified by plotting the correlations between any two parameters, as illustrated in Figure 6. The correlations are fit by using a linear model for both the main and extended emission phases, as well as the entire burst. As shown in Table 3, the slopes between the main and extended emission phases are generally consistent, suggesting that the two phases may share similar radiation mechanisms.

The spectral fits suggest that the synchrotron model is the most likely explanation of GRB 211211A due to the following reasons: (1) As listed in Table 2 and plotted in Figure 5, the values of lower energy photon index,  $\alpha$ , are typically distributed at  $\sim -1.2$  and never exceed the so-called line of death ( $-2/3$ , Preece et al. 1998) of synchrotron radiation. Such an  $\alpha$  distribution is fully consistent with the synchrotron model but not consistent with the simplest photosphere model (e.g.,

**Table 3.** The best-fit parameters of  $\alpha$ ,  $E_p$  and flux  $F$  correlations with linear model.

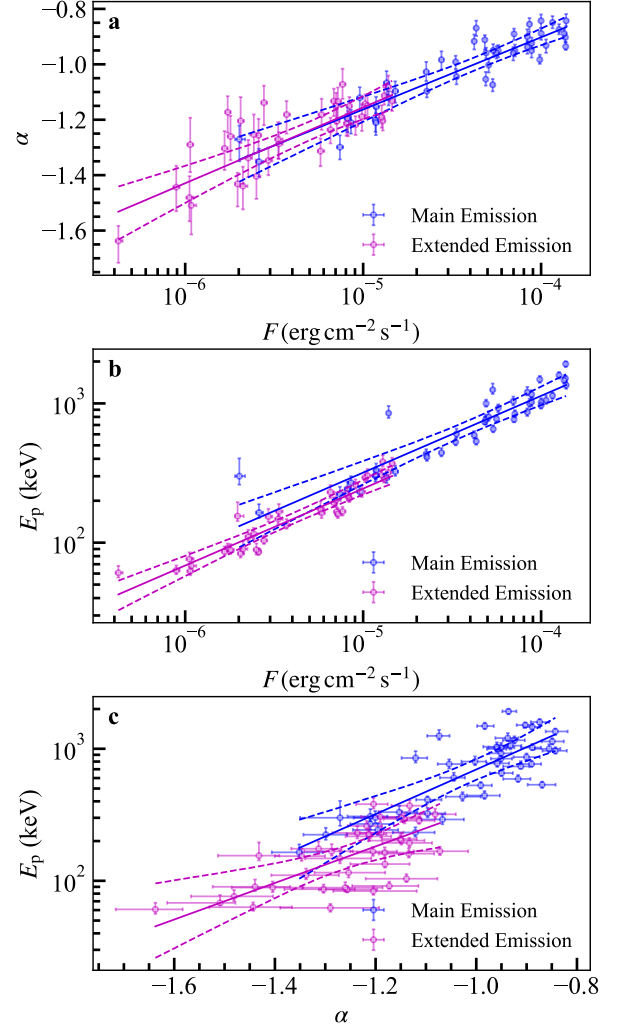
Line model	Main emission		Extended emission		Whole burst	
	$k$	$b$	$k$	$b$	$k$	$b$
$\alpha = k \log F + b$	$0.26^{+0.02}_{-0.02}$	$0.14^{+0.07}_{-0.08}$	$0.27^{+0.03}_{-0.02}$	$0.21^{+0.17}_{-0.11}$	$0.26^{+0.01}_{-0.01}$	$0.15^{+0.05}_{-0.05}$
$\log E_p = k \log F + b$	$0.55^{+0.04}_{-0.03}$	$5.26^{+0.16}_{-0.15}$	$0.55^{+0.05}_{-0.02}$	$5.15^{+0.25}_{-0.10}$	$0.62^{+0.02}_{-0.02}$	$5.53^{+0.08}_{-0.08}$
$\log E_p = k\alpha + b$	$1.69^{+0.20}_{-0.18}$	$4.53^{+0.20}_{-0.19}$	$1.38^{+0.15}_{-0.32}$	$3.92^{+0.20}_{-0.41}$	$2.08^{+0.09}_{-0.14}$	$4.87^{+0.11}_{-0.15}$

**Figure 5.** Distributions of the best-fit  $\alpha$  and  $E_p$  obtained from time-resolved spectral fits.

Mészáros & Rees 2000) which predicts thermal-like spectrum with a much harder  $\alpha$  above the synchrotron death line. To reproduce the soft spectrum as observed, one has to introduce some contrived new ingredients within the photosphere model framework (e.g., Deng & Zhang 2014); (2) The values of the slopes in  $E_p \propto F^k$  relation are  $\sim 0.6$ , which are consistent with predicted relation of  $E_p \propto L^{1/2}$  (e.g., Zhang & Mészáros 2002) by synchrotron models. Comparably, photosphere models predict  $E_p \propto L^{1/4}$  for  $R_{ph} < R_s$ , and  $E_p \propto L^{-5/12}$  for  $R_{ph} > R_s$ , where  $R_{ph}$  is photosphere radius and  $R_s$  is saturation radius (Mészáros & Rees 2000); (3) The  $\alpha$  tracking behavior can be naturally interpreted as synchrotron radiation as suggested by (Uhm & Zhang 2014), and specifically, the one-zone ICMART model (Zhang & Yan 2011).

## 2.2. Host Galaxy

A candidate of the optical counterpart of GRB 211211A is reportedly located very close to an SDSS

**Figure 6.** The  $\alpha$ ,  $E_p$  and flux correlation diagrams. **a**, **b** and **c** show the linear fits to  $\alpha - \log F$ ,  $\log E_p - \log F$  and  $\log E_p - \alpha$  relations during main emission phase (blue) and extended emission (purple) phase. The solid and dashed lines show the best-fit correlations and  $3\sigma$  error bands, respectively.

galaxy (ID: 1237665429707096375<sup>5</sup>) with an offset of  $R_{off} \simeq 5.50''$  (Zheng et al. 2021; Malesani et al. 2021). The r band magnitude of the host galaxy is  $m = 19.53$

<sup>5</sup> <https://skyserver.sdss.org/dr12/en/tools/explore/Summary.aspx?id=1237665429707096375>

mag, with a half-light radius of  $R_{50} = 0.61''$  (exponential model) and photometric redshift of  $z_p = 0.140 \pm 0.0375$  (Adelman-McCarthy et al. 2008). The probabilities of chance coincidence that the afterglow candidates are unrelated to GRB 211211A (defined as  $P_{cc1}$ ) and that this galaxy is independent of the afterglow candidates (defined as  $P_{cc2}$ ) can be calculated as follows. We first assume that the surface distributions of galaxies and GRBs are uniform and follow Poisson distributions (e.g. Bloom et al. 2002; Stalder et al. 2017). The probability of one or more random coincidences is given by

$$P = 1 - e^{-\lambda} \sim \lambda (\lambda \sim 0) \quad (3)$$

where  $\lambda$  is the expectation number of coincidences.

To derive  $P_{cc1}$ ,  $\lambda$  can be regarded as the average number of GRBs occurring within a time window and sky area and is the product of the following three quantities:

- $r_1$ : the detection rate of GRB over the whole sky. The latest *Fermi*/GBM (von Kienlin et al. 2020) and *Swift*/BAT (Lien et al. 2016) burst catalogs provide 236 and 92.2 bursts per year detected by the two instruments, respectively. Considering the facts that 13.6% of *Fermi*/GBM bursts are co-detected by *Swift*/BAT (Narayana Bhat et al. 2016), we estimate a joint detection rate to be  $r_1 \sim 0.8$  bursts per day over the whole sky.
- $r_2$ : the ratio between the localization error circle and the whole sky. Using the the localization uncertainty of  $\theta = 1^\circ$  for GRB 211211A (Fermi GBM Team 2021), one can calculate this ratio to be  $r_2 = (1 - \cos\theta)/2 = 7.62 \times 10^{-5}$ .
- $r_3$ : the time window in which the GRB occurs prior to the optical afterglow. Based on optical afterglow gallery (Kann et al. 2011), we utilize a relatively long time window of one day ( $r_3 = 1$ ) to avoid underestimating  $P_{cc1}$ .

Based on above values, one can calculate  $P_{cc1} \sim \lambda = \Pi_{i=1}^3 r_i$  to be  $6.09 \times 10^{-5}$ . Such probability allow us to rule out a chance coincidence between the the afterglow candidates and the burst at  $4.01\sigma$  confidence level.

For  $P_{cc2}$ ,  $\lambda$  is the expected number of galaxies brighter than  $m$  and within a circle with a radius of  $\Delta R$  and can be derived by the two quantities:

- $\sigma(\leq m)$ : the number density of galaxies brighter than  $m$ . Following Berger (2010), we calculate the number density  $\sigma(\leq m) = 1.6 \times 10^{-4} \text{ arcsec}^{-2}$  based on the results of deep optical galaxy surveys (Hogg et al. 1997; Beckwith et al. 2006), i.e.,

$$\sigma(\leq m) = \frac{10^{0.33(m-24)-2.44}}{0.33 \times \ln(10)} \text{ arcsec}^{-2} \quad (4)$$

- $\Delta R$ : the maximum effective angular radius that the host galaxy is far from the optical counterpart. We take  $\Delta R \approx (R_{\text{off}}^2 + 4R_{50}^2)^{1/2} = 5.63 \text{ arcsec}$  based on the fact that the optical counterpart is outside of the galaxy (Bloom et al. 2002).

Therefore, we calculate  $P_{cc2}$  through  $\lambda = \pi(\Delta R)^2 \sigma(\leq m)$  to be  $1.60 \times 10^{-2}$ , implying a random association between the optical counterpart and the galaxy can be ruled out at  $2.41\sigma$  level.

Finally, the probability of chance coincidence between GRB 211211A and this SDSS galaxy can be calculated by  $P_{cc1} \times P_{cc2} = 9.72 \times 10^{-7}$ , which results in a higher confidence level ( $4.90\sigma$ ) against a random association. Therefore, we take this galaxy as the host galaxy of GRB 211211A.

Malesani et al. (2021) has reported a redshift of  $z_s = 0.076$  based on a weak emission line detected in optical spectroscopy of the host galaxy, which is marginally consistent with the photometric redshift  $z_p = 0.140$ . Assuming the spectroscopic redshift of GRB 211211A is real, and given the angle of  $5.5''$  between GRB 211211A and this host galaxy, the offset in projection can be calculated to be 9.48 kpc. The normalized offset, defined by  $R_{\text{off}}/R_{50}$ , is 9.02. The large offset of GRB 211211A would be very peculiar if it were a Type-II GRB. On the other hand, Type-I GRBs have substantially larger offsets relative to the host galaxies than Type-II GRBs (Bloom et al. 2002; Fong & Berger 2013; Berger 2014), which is in agreement with the prediction of the merger origin of compact binary where each of the compact stars undergoes a supernova “kick” as it forms. The (normalized) offset of GRB 211211A is larger than  $\sim 80\%$  ( $\sim 85\%$ ) of the (normalized) offsets of Type-I GRBs (Fong & Berger 2013). Therefore, GRB 211211A is more likely to originate from a compact star merger event based on its host galaxy information.

### 2.3. Burst Energy

Given a redshift of 0.076, the isotropic energy and peak luminosity of prompt emission of the burst are calculated to be  $E_{\gamma, \text{iso}} = (7.61 \pm 0.11) \times 10^{51} \text{ erg}$  and  $L_{\gamma, p} = 1.94_{-0.03}^{+0.03} \times 10^{51} \text{ erg s}^{-1}$ , respectively.

In Figure 3b, we over-plot GRB 211211A onto the  $E_{p,z} - E_{\gamma, \text{iso}}$  diagram using the type-I and type-II GRBs with known redshift (Amati et al. 2002; Zhang et al. 2009a), where  $E_{p,z} = E_p(1+z)$  is rest-frame peak energy. GRBs of different physical origins typically follow different tracks in such a diagram. We find that the whole burst of GRB 211211A resides in the area between the Type-I and Type-II GRB tracks. It is interesting to note that, similar to GRB 060614, the main emission and the extended emission of GRB 211211A

**Table 4.** The temporal and spectral profiles of X-ray light curves.

Phase	GRB 211211A				GRB 060614			
	start (day)	stop (day)	$\alpha_X$	$\Gamma_X$	start (day)	stop (day)	$\alpha_X$	$\Gamma_X$
I: steep decays	$8.10 \times 10^{-4}$	$2.05 \times 10^{-3}$	$2.98^{+0.03}_{-0.06}$	$1.42^{+0.05}_{-0.05}$	$1.12 \times 10^{-3}$	$2.00 \times 10^{-3}$	$2.47^{+0.06}_{-0.06}$	$1.21^{+0.05}_{-0.05}$
	$2.05 \times 10^{-4}$	$3.42 \times 10^{-3}$	$5.16^{+0.06}_{-0.13}$	$2.48^{+0.06}_{-0.06}$	$2.00 \times 10^{-3}$	$5.37 \times 10^{-3}$	$3.90^{+0.03}_{-0.03}$	$2.28^{+0.04}_{-0.04}$
II: plateau	$4.08 \times 10^{-2}$	$7.48 \times 10^{-2}$	$0.06^{+0.44}_{-0.46}$	$1.54^{+0.13}_{-0.11}$	$5.25 \times 10^{-2}$	$3.83 \times 10^{-1}$	$-0.01^{+0.06}_{-0.03}$	$1.71^{+0.11}_{-0.04}$
III: normal decay	$7.48 \times 10^{-2}$	$7.88 \times 10^{-1}$	$1.59^{+0.11}_{-0.12}$	$1.50^{+0.18}_{-0.09}$	$3.83 \times 10^{-1}$	$1.74 \times 10^0$	$1.39^{+0.03}_{-0.18}$	$1.85^{+0.13}_{-0.12}$
IV: post jet-break decay	$7.88 \times 10^{-1}$	$1.94 \times 10^0$	$3.48^{+0.43}_{-0.54}$	$1.41^{+0.55}_{-0.29}$	$1.74 \times 10^0$	$2.35 \times 10^1$	$2.05^{+0.04}_{-0.12}$	$1.64^{+0.22}_{-0.19}$

are located differently. As can be seen from Figure 3b, the main emission of GRB 211211A follows the track of Type-I GRBs, while the extended emission follows the track of Type-II GRBs. We note that the locations of GRB 211211A are systemically higher than those of GRB 060614 in the Amati relation, suggesting that, although the two bursts may share similar physical origins, GRB 211211A poses a higher total energy and harder spectra in both the main and extended phases.

#### 2.4. Multi-wavelength Afterglow

##### 2.4.1. X-ray Afterglow

The *Swift* X-ray Telescope (XRT; Burrows et al. 2005) began to observe the BAT field from 69 s after the BAT trigger and identified a bright, uncatalogued X-ray source located at RA=14<sup>h</sup>09<sup>m</sup>10.09<sup>s</sup> and DEC=+27°53′18.8″ (J2000) with an uncertainty of 2.1″ (Beardmore et al. 2021). Figure 7 shows the X-ray light curve and photon index evolution of GRB 211211A obtained from *Swift*-XRT GRB lightcurve repository<sup>6</sup> and *Swift*-XRT GRB spectrum repository<sup>7</sup>, respectively. Note that we convert the 0.3-10 keV flux into the 1 keV flux density using the time-averaged photon index for each of both the Windowed Timing (WT) mode and Photon Counting (PC) mode. Due to the long gap between the WT mode and PC mode, we fit the light curves in WT and PC modes separately using a multi-segment broken-power-law (BPL) model<sup>8</sup>. The fitting process is implemented by the python module *emcee* (Foreman-Mackey et al. 2013). Based on the Bayesian information criterion<sup>9</sup> (BIC), the light curve in WT mode can be modeled by two power-law segments. For

the light curve in PC mode, the 3-segment BPL model provides a better fit (stat/dof=45.58/46, BIC=69.29) than the 2-segment BPL model fit (stat/dof=56.22/48, BIC=72.02). Based on our fits, the X-ray light curve of GRB 211211A can be divided into four phases. The time range, power-law decay index of the light curve ( $\alpha_X$ ), and photon index of the spectrum ( $\Gamma_X$ ) of each phase are listed in Table 4. These four phases match up well with a canonical GRB X-ray light curve (Zhang et al. 2006; Nousek et al. 2006). Details of each phase are further itemized below.

- Phase I – the steep decay. The sharp decay slopes ( $\alpha_X \geq 3$ ) and strong spectral evolution can be interpreted by the higher latitude effect (Kumar & Panaitescu 2000; Dermer 2004) of the tail of the prompt emission with an intrinsically curved spectral shape (Zhang et al. 2007b, 2009b).
- Phase II – the shallow decay. With a decay index  $\alpha_X \sim 0$ , Phase II is a well-defined plateau, as seen in many previous GRB X-ray light curves. Physically speaking, X-ray plateaus can be divided into two categories, namely, external plateaus and internal plateaus. The external plateau is followed by a normal decay phase and can be interpreted by invoking a continuous energy injection caused by a long-lasting central engine (Dai & Lu 1998; Zhang & Mészáros 2001a) or stratified ejecta (Rees & Mészáros 1998; Sari & Mészáros 2000) within the external forward shock model (Zhang et al. 2006; Nousek et al. 2006). The internal plateaus are usually followed by a late-time steep decay segment and are inconsistent with the standard external shock model. One has to introduce an internal dissipation process (e.g., formation of a black hole from a magnetar; Troja et al. 2007; Lyons et al. 2010) to explain the sudden change of decay slopes. The plateau of GRB 211211A fits the former case as it is followed by a normal decay phase, and no significant spectral evolution is observed between the two phases (Figure 7b). This suggests that Phase II is likely powered by the con-

<sup>6</sup> [https://www.swift.ac.uk/xrt\\_curves/](https://www.swift.ac.uk/xrt_curves/)

<sup>7</sup> [https://www.swift.ac.uk/xrt\\_spectra/](https://www.swift.ac.uk/xrt_spectra/)

<sup>8</sup> A convention of  $f_\nu \propto t^{-\alpha_X} \nu^{-\Gamma_X+1}$  is employed here, where  $\alpha_X$  is the decay slope of the light curve and  $\Gamma_X$  is defined as the photon index of the X-ray spectrum.

<sup>9</sup> Bayesian information criterion (Schwarz 1978) is defined as  $BIC = -2\ln\mathcal{L} + k\ln N$ , where  $\mathcal{L}$  is the maximum likelihood,  $k$  is the number of parameters of model, and  $N$  is the number of data points.

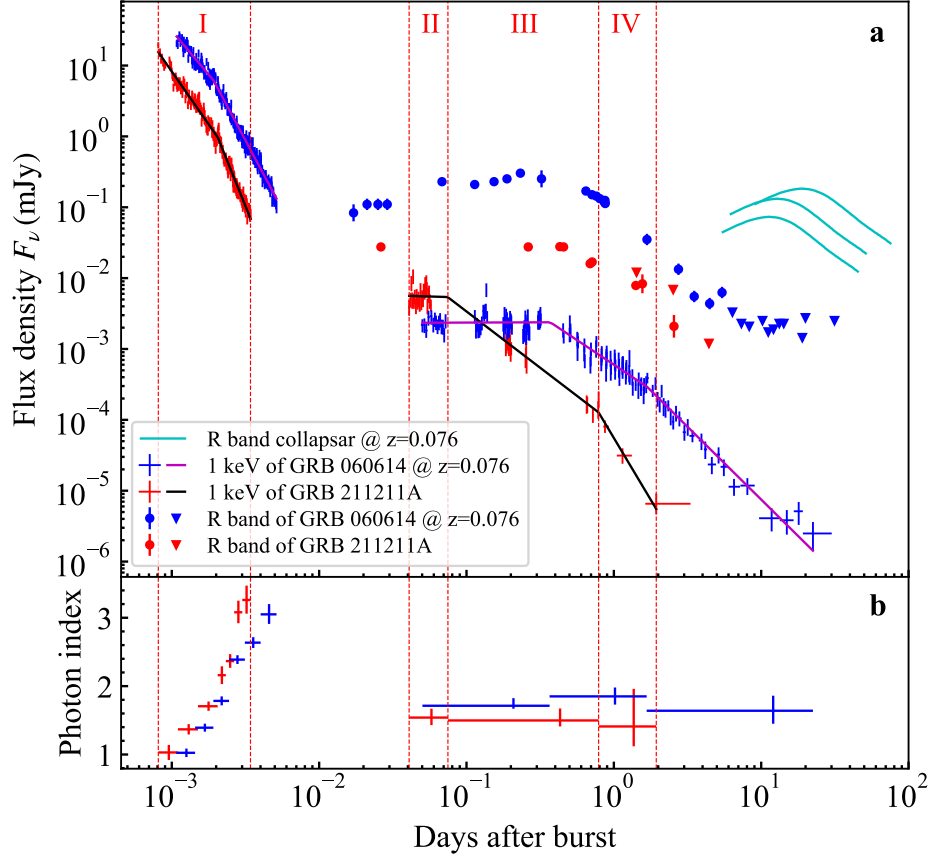


**Figure 7.** **a**, The X-ray (1 keV) and R band afterglows, and the R band collapsar. The observed (modeled with the BPL model) X-ray light curves for GRB 211211A and GRB 060614 are shown with red pluses (magenta lines) and blue pluses (black lines), respectively. The R band observations for GRB 211211A and GRB 060614 are shown with red and blue squares (down triangles for upper limits), respectively. The cyan lines represent the R band collapsars, including SN 1998bw/GRB 980425, SN 2006aj/GRB 060218A, SN 2010bh/GRB 100316D. The vertical red dashed lines are drawn at the edges of each phase in the X-ray light curve of GRB 211211A. **b**, The evolution of X-ray photon index of GRB 211211A (red pluses) and GRB 060614 (blue pluses).

tinuous energy injection of the GRB central engine (Zhang et al. 2006; Nousek et al. 2006).

- Phase III – the normal decay. With  $\alpha_X = 1.59$  and  $\Gamma_X = 1.50$ , the normal decay phase is well consistent with the prediction of the standard external shock afterglow model (e.g., Racusin et al. 2009).
- Phase IV – post jet-break decay. A break appears at  $\sim 0.8$  days, a typical time as a jet break. The break is followed by a slightly steeper decay phase with  $\alpha_X \sim 3.5$  that lasts till  $\sim 2$  days. As modeled in §3.1, we found an off-axis afterglow from a structured jet succeeds in interpreting the observed data.

Comparatively, we analyze the *Swift*-XRT light curve for GRB 060614 and present the fitting results in Table 4. We rescale its light curve to the redshift of GRB

211211A and over-plot it in Figure 7. Both bursts exhibit similar temporal and spectral characteristics in the X-ray band. Nevertheless, the X-ray flux of GRB 211211A is generally weaker than that of GRB 060614, except during the plateau phase, when the energy injection of GRB 211211A is stronger but lasts for a shorter period of time.

#### 2.4.2. Ultraviolet, Optical and Near-infrared Afterglows

In order to model multi-wavelength afterglows, we collect all ultraviolet, optical, and near-infrared observations at the *Swift*-XRT coordinate as listed in Table 5. The *Swift* Ultraviolet and Optical Telescope (UVOT; Roming et al. 2005) performed five rounds of observations in the field of GRB 211211A from 92 seconds to  $\sim 3$  days after the BAT trigger. The UVOT data are

**Table 5.** Ultraviolet, optical and near-infrared observations of GRB 211211A.

$T - T_0$ (day)	Telescope	Band	AB Magnitude	Ref. <sup>a</sup>
0.026	KAIT	Clear ( $\sim$ R)	$20.30 \pm 0.20^b$	(1)
0.042	Swift/UVOT <sup>c</sup>	U	$19.86 \pm 0.15$	(2)
0.044	Swift/UVOT	B	$19.74 \pm 0.23$	(2)
0.049	Swift/UVOT	UVW2	$19.74 \pm 0.15$	(2)
0.051	Swift/UVOT	V	$19.27 \pm 0.30$	(2)
0.053	Swift/UVOT	UVM2	$19.79 \pm 0.18$	(2)
0.056	Swift/UVOT	UVW1	$19.55 \pm 0.14$	(2)
0.057	Swift/UVOT	U	$19.56 \pm 0.19$	(2)
0.186	Swift/UVOT	U	$19.76 \pm 0.12$	(2)
0.190	Swift/UVOT	U	$19.83 \pm 0.12$	(2)
0.193	Swift/UVOT	U	$19.99 \pm 0.14$	(2)
0.196	Swift/UVOT	B	$19.95 \pm 0.26$	(2)
0.200	Swift/UVOT	B	$20.03 \pm 0.33$	(2)
0.254	Swift/UVOT	UVM2	$20.63 \pm 0.17$	(2)
0.263	MITSuME/Akeno	Ic	$20.40 \pm 0.30$	(3)
0.263	MITSuME/Akeno	Rc	$20.30 \pm 0.10$	(3)
0.263	MITSuME/Akeno	g'	$20.40 \pm 0.20$	(3)
0.430	Nanshan/NEXT	r	$20.29 \pm 0.07$	(4)
0.445	Nanshan/NEXT	z	$19.90 \pm 0.30$	(4)
0.456	HCT	R	$20.30 \pm 0.13$	(5)
0.655	CAFOS/CAHA	i	$20.83 \pm 0.05$	(6)
0.656	Swift/UVOT	UVW1	$21.93 \pm 0.27$	(2)
0.663	Swift/UVOT	U	$> 20.62$	(2)
0.690	NOT	r	$20.89 \pm 0.05$	(7)
0.713	LCO	R	$20.83 \pm 0.09$	(8)
0.713	LCO	I	$21.49 \pm 0.25$	(8)
0.720	Swift/UVOT	UVW2	$22.30 \pm 0.28$	(2)
0.726	Swift/UVOT	V	$> 19.34$	(2)
0.784	Swift/UVOT	B	$> 20.66$	(2)
0.852	Swift/UVOT	UVW1	$22.18 \pm 0.31$	(2)
0.858	Swift/UVOT	U	$> 20.89$	(2)
0.917	Swift/UVOT	UVW2	$> 22.75$	(2)
0.923	Swift/UVOT	V	$> 19.37$	(2)
1.049	Swift/UVOT	B	$> 20.66$	(2)
1.126	Swift/UVOT	UVW1	$> 22.10$	(2)
1.182	Swift/UVOT	U	$> 21.39$	(2)
1.259	Swift/UVOT	UVM2	$> 22.31$	(2)
1.321	Swift/UVOT	UVW1	$> 22.13$	(2)
1.396	GMG	r	$> 22.00$	(9)
1.410	Devasthal	R	$21.66 \pm 0.07$	(10)
1.425	GIT	r'	$> 21.19$	(5)
1.562	AbAO	R	$21.60 \pm 0.33$	(11)
1.650	CAFOS/CAHA	i	$22.45 \pm 0.09$	(12)
2.527	AbAO	R	$> 21.80$	(11)
2.558	SAO RAS	Rc	$23.10 \pm 0.40$	(13)
2.912	Swift/UVOT	UVM2	$> 22.77$	(2)
4.000	Gemini/NIRI	K	$22.40 \pm 0.10$	(14)
4.420	Devasthal	R	$> 23.70$	(10)
4.700	TNG/NICS	H	$> 21.90$	(15)
6.900	MMT/MMIRS	K	$24.00 \pm 0.20^d$	(16)

NOTE—

a: (1): GCN Circular 31203; (2): Swift quick look data; (3): GCN Circular 31217; (4): GCN Circular 31213; (5): GCN Circular 31227; (6): GCN Circular 31218; (7): GCN Circular 31221; (8): GCN Circular 31214; (9): GCN Circular 31232; (10): GCN Circular 31299; (11): GCN Circular 31233; (12): GCN Circular 31228; (13): GCN Circular 31234; (14): GCN Circular 31235; (15): GCN Circular 31242; (16): GCN Circular 31264.

b: The magnitude error is derived by assuming a signal-to-noise ratio of  $5\sigma$ .

c: For Swift/UVOT observations, we exclude the detections of white filter, and only list the tightest upper limit when several time bins are very close together.

d: The magnitude error is derived by assuming a signal-to-noise ratio of  $5\sigma$ .

obtained from *Swift* archive website<sup>10</sup>. The white filter data in UVOT observations was excluded from this study due to its flat transmission function. Additionally, we only employ the tightest upper limit when several time bins are very close together. The detections and upper limits reported in GCN circulars<sup>11</sup> by multiple facilities are also collected in Table 5.

Compared with the X-ray light curve, the R band light curve is over-plotted in Figure 7. The initial 11-hour photometric data does not show significant decay. Afterwards, it decays as a power-law with an index of 1.00 until 1.56 days. The final two detections in R band indicate a fast power-law decay with an index of 2.80. We also collected the R band light curve of GRB 060614 from the literature (Gal-Yam et al. 2006; Fynbo et al. 2006) and over-plotted it in Figure 7 by rescaling it to the redshift of GRB 211211A. In comparison to GRB 060614, the optical afterglow of GRB 211211A has a similar temporal profile but is generally weaker by about one order of magnitude. Regarding multi-band behavior, GRB 060614 appears to behave normally, whereas GRB 211211A shows a significant chromatic feature, that is, the light curves of different bands break at different times. Given that the breaks themselves are not of spectral origins (see §2.4.1), the chromatic behavior cannot be interpreted by the standard external shock afterglow model, which predicts achromatic breaks. We will further show the deviation between the afterglow data and the standard model by modeling the multi-wavelength afterglows in 3.1.

A robust association between Type-II GRBs and SNe has been established, and the smoking gun signature is the detection of characteristic spectral features of the supernova in the optical afterglow (Galama et al. 1998; Reeves et al. 2002; Hjorth et al. 2003). With a redshift of 0.076, if GRB 211211A were a Type-II GRB, a significant supernova component would be expected approximately ten days later. To examine the possibility of an association between GRB 211211A and a supernova, we obtain the quasi-bolometric unreddened rest-frame light curves of SN 1998bw from Clocchiatti et al. (2011). We then apply a scale factor,  $k$ , and a stretch factor,  $s$ , to the template supernova, SN 1998bw, in order to obtain a specific supernova light curve. The observed flux density at redshift  $z$  of the specific supernova can be described

<sup>10</sup> <https://www.swift.ac.uk/archive/ql.php>

<sup>11</sup> <https://gcn.gsfc.nasa.gov/other/211211A.gcn3>

**Table 6.** The best-fit parameters of the modelings for multi-wavelength observations.

Model	$\log_{10} E_{k, \text{iso}}$ (erg)	$\theta_v$ (rad)	$\theta_c$ (rad)	$\log_{10} n$ (cm $^{-3}$ )	$p$	$\log_{10} \epsilon_e$	$\log_{10} \epsilon_B$	$\kappa^1$ (cm $^2$ g $^{-1}$ )	$M_{\text{ej}}^1$ (M $_{\odot}$ )
AG	$51.697^{+0.787}_{-0.342}$	$0.067^{+0.018}_{-0.037}$	$0.035^{+0.035}_{-0.014}$	$-1.069^{+1.230}_{-0.364}$	$2.201^{+0.095}_{-0.018}$	$-0.848^{+0.156}_{-0.834}$	$-2.563^{+0.051}_{-1.078}$	...	...
AG+KN	$52.698^{+0.255}_{-0.901}$	$0.089^{+0.030}_{-0.025}$	$0.038^{+0.026}_{-0.005}$	$0.691^{+0.703}_{-1.086}$	$2.228^{+0.050}_{-0.034}$	$-1.468^{+0.771}_{-0.270}$	$-4.145^{+0.756}_{-0.576}$	$0.660^{+0.090}_{-0.218}$	$0.038^{+0.006}_{-0.003}$
AG+2KN	$51.951^{+0.597}_{-0.237}$	$0.100^{+0.021}_{-0.037}$	$0.056^{+0.020}_{-0.012}$	$0.876^{+0.607}_{-0.761}$	$2.171^{+0.053}_{-0.007}$	$-0.559^{+0.058}_{-0.832}$	$-4.728^{+0.757}_{-0.102}$	$3.584^{+0.602}_{-1.634}$	$0.033^{+0.001}_{-0.007}$

$v_{\text{ej}}^1$ (c)	$T^1$ (K)	$\kappa^2$ (cm $^2$ g $^{-1}$ )	$M_{\text{ej}}^2$ (M $_{\odot}$ )	$v_{\text{ej}}^2$ (c)	$T^2$ (K)	$\log_{10} E(B - V)$	$\log_{10} v$ (mag)	stat/dof	BIC
...	...	...	...	...	...	$-2.356^{+0.744}_{-0.311}$	$-1.792^{+0.645}_{-0.389}$	2889.02/41	2924.23
$0.252^{+0.050}_{-0.047}$	$1602.787^{+922.317}_{-699.570}$	...	...	...	...	$-3.035^{+1.230}_{-0.447}$	$-0.781^{+0.114}_{-0.116}$	20.46/37	71.32
$0.327^{+0.006}_{-0.100}$	$377.443^{+1994.530}_{-275.032}$	$0.192^{+0.054}_{-0.071}$	$0.037^{+0.006}_{-0.013}$	$0.295^{+0.016}_{-0.070}$	$9898.060^{+101.863}_{-2673.298}$	$-3.358^{+1.364}_{-0.192}$	$-0.925^{+0.141}_{-0.032}$	3.46/33	69.97

as

$$F_{\nu}^{\text{SN}}(t_{\text{obs}}, \nu_{\text{obs}}) = \frac{(1+z)k}{4\pi d_L^2} L_{\nu}^{\text{SN}} \left( \frac{t_{\text{obs}}}{(1+z)s}, (1+z)\nu_{\text{obs}} \right) \quad (5)$$

where  $d_L$  is luminosity distance and  $L_{\nu}^{\text{SN}}$  is specific luminosity at frequency  $\nu$  of template supernova. In Figure 7 we demonstrate the R band light curves of three well-studied supernovae associated with long GRBs, including the template SN 1998bw/GRB 980425, SN 2006aj/GRB 060218A ( $s = 0.68$  and  $k = 0.72$ ; Cano 2013) and SN 2010bh/GRB 100316D ( $s = 0.60$  and  $k = 0.40$ ; Cano 2013), by putting them at the redshift of GRB 211211A. The three supernovae cover a considerable range of luminosity, with SN 1998bw and SN 2010bh ranked the brightest and faintest GRB-SNs, respectively. Similar to GRB 060614, the R band afterglow of GRB 211211A decays so rapidly that at 4-5 days, it is about two orders of magnitude fainter than the supernovae at this time, and there is still no sign of a supernova bump. The absence of a supernova associated with GRB 211211A rules out this being a typical Type-II GRB produced by the core collapse of a massive star.

### 3. IDENTIFICATION OF A KILONOVA

Type-I GRBs are believed to originate from the merger of a compact binary, specifically, a neutron star-neutron star or neutron star-black hole merger. During the coalescence, a considerable amount of the neutron-rich materials would be ejected, either due to the dynamical process of the merger (Lattimer & Schramm 1974; Rosswog et al. 1999; Rosswog 2005; Hotokezaka et al. 2013; Kyutoku et al. 2013), or due to the winds from the accretion disk surrounding the central remnant (Dessart et al. 2008; Metzger & Fernández 2014). The r-process nucleosynthesis can generate heavy elements, and the  $\beta$  decay can heat the ejecta and power nearly isotropic thermal radiation, known as a kilonova (Li & Paczyński 1998; Metzger et al. 2010). The kilonovae

are usually observed one to a few days after the Type-I GRBs in the ultraviolet, optical and near-infrared bands (Tanvir et al. 2013; Berger et al. 2013; Fan et al. 2013; Abbott et al. 2017). Hence, the kilonova components superposed on the light curves of UV/optical/near-IR afterglows can be used to assess the compact-binary nature of a GRB.

In this section, we fit the observed multi-wavelength light curves with both the afterglow-only (AG-only) and the afterglow plus kilonova (AG+KN) models. Details of the methods are provided below.

#### 3.1. Fit with AG-only Model

The theoretical afterglow light curves are generated using the public python package *Afterglowpy*, (Ryan et al. 2020), which can compute external forward shock synchrotron radiation and handle both the structured jet and off-axis-observer cases. We apply a Gaussian structured jet for our calculation. A model-dependent set of input parameters includes the isotropic kinetic energy ( $E_{k, \text{iso}}$ ), viewing angle ( $\theta_v$ ), Gaussian width of jet core ( $\theta_c$ ), circumburst density ( $n$ ), electron energy distribution index ( $p$ ), and the fractions of shock energy that go to electrons ( $\epsilon_e$ ) and magnetic fields ( $\epsilon_B$ ). For a Gaussian structured jet, we provide a sensible value  $4\theta_c$  to truncate the outer regions of the jet.

To correct the data in Table 5 for foreground Galactic extinction on the line of sight, we applied the F99 (Fitzpatrick 1999) model with a visual extinction to reddening ratio  $R_V = 3.1$  to extinguish the flux density of afterglow model, which is implemented with the *dust-extinction* python package (Astropy Collaboration et al. 2013). We leave the color excess  $E(B - V)$  as a free parameter during the procedure.

The fitting of the observational data are based on the nested sampling algorithm, by applying the Bayesian computation python package *PyMultinest* (Buchner

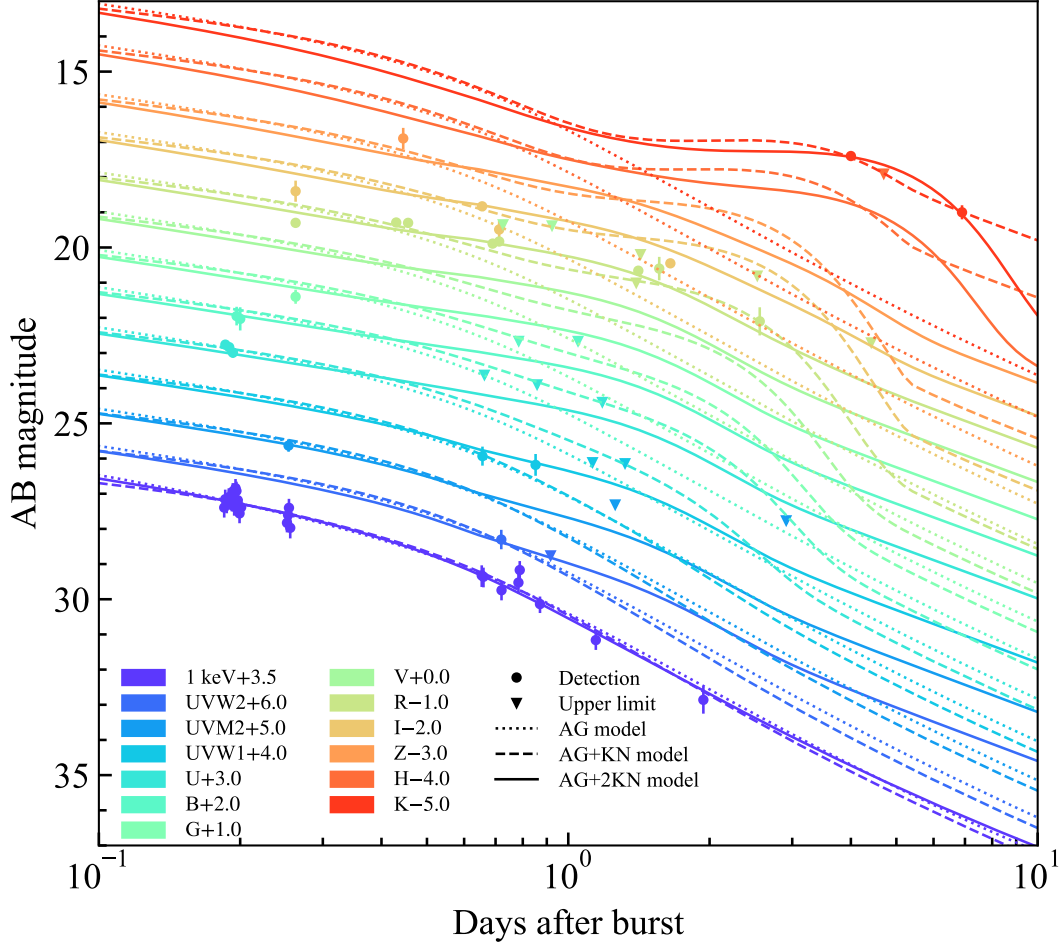


**Figure 8.** The multi-wavelength observations and best-fit models. The detections and upper limits of the multi-wavelength data are shown with circles and down-triangles, respectively. The best-fit AG-only, AG+KN, and AG+2KN models are shown with dotted, dashed, and solid lines, respectively.

et al. 2014), with the log-likelihood function written as

$$\ln \mathcal{L} = -\frac{1}{2} \sum_{i=1}^n \left[ \frac{(O_i - M_i)^2}{\sigma_i^2 + v^2} - \ln [2\pi(\sigma_i^2 + v^2)] \right] \quad (6)$$

where  $O$ ,  $M$ , and  $\sigma$  stand for the observed magnitudes, modeled magnitudes, and uncertainties of observed magnitudes, respectively. The subscript  $i$  represents the serial number for each observational and modeled value. An extra variance parameter  $v$  is introduced to account for the variance of Gaussian distribution, which encompasses additional uncertainty in observed data. We utilize  $-2\ln \mathcal{L}$  as a statistic to measure the goodness of modeling. To avoid the effect of energy injection, we only consider the afterglow after the X-ray plateau. Then we allow all model parameters to vary with typical but broad priors to search for the best fit for observed data.

Firstly, we fit all the observational data, from X-ray to near-infrared, with the AG-only model. We find that

significant residual errors exist even with the best-fitting parameters, especially in the R-band and near-infrared light curves.

Then, we exclude the observation data in R, I, and K bands and fit the rest again with the AG-only model. The best-fit parameters with  $1\sigma$  uncertainties, as well as the corresponding statistic values, are listed in Table 6. Considering the highly degenerate nature of the parameters in the afterglow model, two pairs of parameters,  $E_{k,iso}$  and  $\epsilon_e$ ,  $n$  and  $\epsilon_B$ , are poorly constrained, but are in general consistent with the statistical results in Wang et al. (2015). With the aid of a clearly visible jet break in the X-ray afterglow, the jet opening angle  $\theta_c$  can be well constrained. The viewing angle  $\theta_v \sim 2\theta_c$  indicates that this burst was seen in a slightly off-axis manner. The AG-only model explains the overall trends of the multi-wavelength light curves, in particular in the X-ray band. Nonetheless, significant disagreement between the observational data and the afterglow model

at  $t > 1$  day is observed in the R, I, and K bands, as plotted in Figure 8. These significant excesses result in poor statistics and high BIC values, as shown in Table 6, indicating that other emission components are required to explain the observed data.

### 3.2. Fits with AG+KN Models

The light curve of kilonova emission highly depends on the mass ( $M_{\text{ej}}$ ) and opacity ( $\kappa$ ) of the ejecta. The mass determines how much thermal energy may be generated from the radioactive heating, while the opacity significantly influences the radiation transfer process and the subsequent thermal emission. An ejecta component with a higher electron fraction tends to have a higher opacity. Such an effect can lead to pushing the bolometric light curve to peak later and shifting the spectral peak to redder wavelengths (Kasen et al. 2013; Barnes & Kasen 2013), which can be approximately formulated as  $t_{\text{peak}} \propto \kappa^{1/2}$  and  $T_{\text{peak}} \propto \kappa^{-3/8}$  (Li & Paczyński 1998; Metzger et al. 2010). One of the most well observed kilonova events is AT2017gfo associated with GW170817 and GRB 170817A, which is believed to be originated from a binary NS merger. There are two components on the light curves of the kilonova identified in AT2017gfo, namely the “blue” and “red” components (e.g. Arcavi et al. 2017; Chornock et al. 2017; Cowperthwaite et al. 2017; Drout et al. 2017; Evans et al. 2017; Gao et al. 2017; Kasen et al. 2017; Kilpatrick et al. 2017; Nicholl et al. 2017; Pian et al. 2017; Shappee et al. 2017; Smartt et al. 2017; Tanvir et al. 2017; Villar et al. 2017). The blue component corresponds to a lower opacity and peaks about half a day after the merger (Chornock et al. 2017; Cowperthwaite et al. 2017; Gao et al. 2017; Kasen et al. 2017; Kilpatrick et al. 2017; Shappee et al. 2017; Tanvir et al. 2017; Villar et al. 2017). Later, the blue component fades away, and the red component becomes dominant, which has lasted for tens of days after the burst (Arcavi et al. 2017; Coulter et al. 2017; Cowperthwaite et al. 2017; Drout et al. 2017; Evans et al. 2017; Gao et al. 2017; Kasen et al. 2017; Kilpatrick et al. 2017; Nicholl et al. 2017; Pian et al. 2017; Smartt et al. 2017; Villar et al. 2017). The multi-component behavior of the kilonova transient has been seen in both photometric (Villar et al. 2017) and spectroscopic (Chornock et al. 2017) observations.

Motivated by the similarities between GRBs 211211A and 060614, we investigated the afterglow plus kilonova model to explain the significant excess observed in the optical and near-infrared bands of GRB 211211A. The exact mock observation of kilonova at a specific distance, time, and energy band is generated by the kilonova model described in Villar et al. (2017), which is

packaged in the python library *MOSFIT* (Guillochon et al. 2018). We investigate the one-component (KN) as well as the two-component (2KN) kilonova models in addition to the afterglow (AG) model (see §3.1) to fit to the observed data. In our calculation, each kilonova component is evolved independently and characterized by four free parameters: opacity ( $\kappa$ ), ejecta mass ( $M_{\text{ej}}$ ), ejecta velocity ( $v_{\text{ej}}$ ), and temperature floor ( $T$ ).

Fitting both models (AG+KN and AG+2KN) to the multi-wavelength observations, the best-fit parameter values and their  $1\sigma$  uncertainties are presented in Table 6. The modeled light curves are also plotted as dashed and solid lines in Figure 8. The best-fitting afterglow parameters in AG+KN and AG+2KN models are consistent with those in the AG-only model when considering the degenerate nature. Kilonova models are successful in fitting to the excesses in R and infrared bands as evidenced by significant decreases in statistics and BICs in Table 6.

As for the AG+KN model, the best-fitting parameters of the one-component kilonova are  $\kappa = 0.660^{+0.090}_{-0.218} \text{ cm}^2 \text{ g}^{-1}$ ,  $M_{\text{ej}} = 0.038^{+0.006}_{-0.003} M_{\odot}$ ,  $v_{\text{ej}} = 0.252^{+0.050}_{-0.047} c$  and  $T = 1602.787^{+922.317}_{-699.570} \text{ K}$ . Such a kilonova component is similar to the blue component in the kilonova accompanying the binary neutron star merger GW170817 (e.g. Villar et al. 2017). Although this model provides an adequate fit, it over-predicts some of the R band data within 0.5 – 2.0 days and under-predicts the I band data at 1.65 days.

On the other hand, the two-component kilonova model, AG+2KN, provides the minimum statistic and BIC, although its complexity of 17 free parameters naturally leads to significant over-fitting (stat/dof < 1). In comparison with the AG+KN model, this model is able to better predict the data. The corresponding corner plot is shown in Figure 9. The best-fitting parameters for the red kilonova component are  $\kappa_{\text{red}} = 3.584^{+0.602}_{-1.634} \text{ cm}^2 \text{ g}^{-1}$ ,  $M_{\text{ej,red}} = 0.033^{+0.001}_{-0.007} M_{\odot}$ ,  $v_{\text{ej,red}} = 0.327^{+0.006}_{-0.100} c$  and  $T_{\text{red}} = 377.443^{+1994.530}_{-275.032} \text{ K}$ . The best-fitting parameters for the blue kilonova component are  $\kappa_{\text{blue}} = 0.192^{+0.054}_{-0.071} \text{ cm}^2 \text{ g}^{-1}$ ,  $M_{\text{ej,blue}} = 0.037^{+0.006}_{-0.013} M_{\odot}$ ,  $v_{\text{ej,blue}} = 0.295^{+0.016}_{-0.070} c$ , and  $T_{\text{blue}} = 9898.060^{+101.863}_{-2673.298} \text{ K}$ . Such a opacity corresponds to the blue kilonova component following GW170817 (e.g. Villar et al. 2017). We note that the blue component here is less opaque than that of AT2017gfo (e.g. Villar et al. 2017).

The kilonova components can be further revealed by subtracting the AG components from the model and data, as shown in Figure 10. The AG-free multi-wavelength KN light curves rise rapidly in the early times, followed by a significant peak occurring at about 0.7 days across all bands. A second bump-like peak oc-

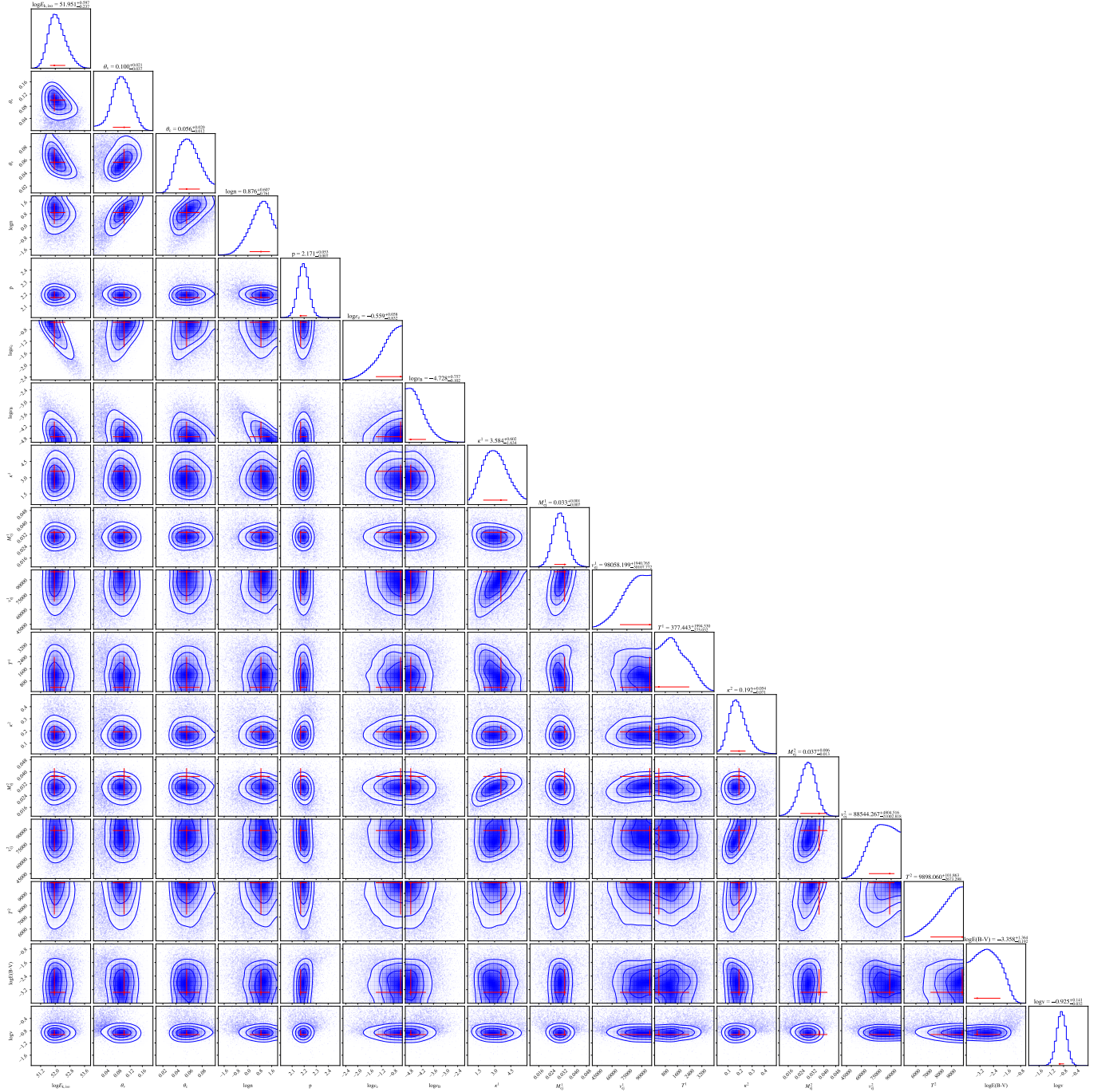


**Figure 9.** Corner plot of the posterior probability distributions of the parameters for the fit of AG+2KN model to multi-wavelength data. The red error bars represent  $1\sigma$  uncertainties.

curs at about four days and is present only in the H and K bands.

In Figure 11, we plot the light curves of two KN components in four different representative filters of the optical band. Clearly, the blue kilonova component dominates across all bands at  $\lesssim 1$  day and contributes to the first peak in Figure 10. In later times, the blue component contributes most of the emission in ultraviolet

and optical bands, while the red KN component only dominates across the redder (H and K) bands.

#### 4. NATURE OF THE BURST

The following evidence, ranked in order of importance, suggests that GRB 211211A is a merger event:

1. Presence of a kilonova and absence of a supernova;

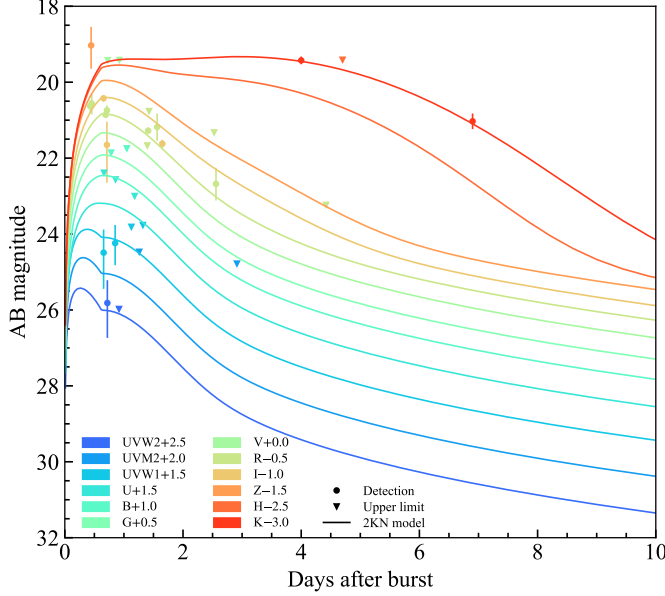


**Figure 10.** Afterglow-subtracted multi-wavelength observations of GRB 211211A and best-fit results with 2KN model. Solid lines are the best-fit models in different optical bands.

2. ME+EE temporal structure, which has been observed in some previous Type-I GRBs, such as GRB 060614;
3. ME being consistent with a Type-I GRB in Amati relation;
4. Tiny lags measured in the prompt emission, suggesting a small emission region, as expected by a merger-type GRB central engine;
5. Large offset of burst location in its host galaxy, consistent with a merger-type event due to the kick history;
6. Existence of a plateau in the X-ray light curve w/o late-time sharp decay, consistent with a magnetar-powered central engine, which can be a product of a NS-NS merger event.

However, the genuine long duration of the burst makes it an unprecedented case compared to any other merger-type GRBs. In particular, the long duration and hard spectra over the whole burst are not attributable to the instrumental sensitivity and soft tail of the prompt emission, as it is the case of GRB 060614. This poses a challenge to the merger model in terms of how to produce a GRB lasting for over 50 s.

An option for overcoming the dilemma is to invoke differential-rotation-induced magnetic bubbles as the mechanism for producing GRB prompt emission (Kluźniak & Ruderman 1998; Ruderman et al. 2000;

Dai et al. 2006; Zhang et al. 2021), assuming the merger product is a magnetar. This model invokes magnetic bubble eruptions from the magnetar surface and naturally produces a temporal profile consisting of several spikes (or sub-bursts) with large fluctuations. In such a model, the duration of a GRB is dependent on the number of bubbles and the interval between two bubble eruptions. Each magnetic bubble eruption follows the same process as described below.

We consider a differentially rotating magnetar with an internal poloidal magnetic field  $B_r = 10^{13}$  G and an initial spin period  $P_0 \sim 1$  ms. Here we take the convention that  $Q_x = Q/10^x$  and all the quantities are in *cgs* unit system. Due to differential rotation,  $B_r$  will be wound up into a toroidal magnetic field  $B_\phi$  which increases as  $dB_\phi/dt = \Delta\Omega B_r$  (Dai et al. 2006), where  $\Delta\Omega$ , with an initial value of  $2\pi/P_0$ , is the differential angular velocity between the inner and outer parts of magnetar. Continually amplified  $B_\phi$  forms a magnetically confined toroid inside the magnetar to enclose some matter. When  $B_\phi$  is amplified to a critical magnetic field  $B_b \approx 10^{17}$  G (Kluźniak & Ruderman 1998), the magnetic buoyant force can balance the antibuoyant stratification in magnetar composition, which corresponds to a critical time scale  $\tau_b = B_b/(\Delta\Omega B_r) \simeq 1.6 \times B_{r,13}^{-1} P_{0,-3}$  s. Such a time scale corresponds to the interval between two bubble eruptions. As  $B_\phi$  continues to increase after  $\tau_b$ , the buoyancy force will exceed the antibuoyant force. The magnetic toroid becomes unstable and floats up toward the magnetar surface due to excess buoyancy. The buoyancy time scale, during which the magnetic toroid floats up and penetrates through the magnetar surface, can be calculated as  $\Delta\tau_b \simeq 8.4 \times B_{r,13}^{-1/3} P_{0,-3}^{1/3}$  ms. Upon penetration through the magnetar surface, the toroidal fields may reconnect and give rise to an explosive event with energy  $E_b \simeq 1.6 \times 10^{51}$  erg. Such a reconnection process typically occurs within  $\sim 10^{-4}$  s, corresponding to the large fluctuations as observed in the observations. Once this event is over, a similar process described above will lead to another explosion as long as  $\Delta\Omega$  remains large enough. A magnetar with an initial kinetic energy of  $10^{53}$  erg is capable of producing  $\sim 10$  similar eruptions (Kluźniak & Ruderman 1998). This yields a total duration of  $\sim 16$  s, which is in agreement of the observed duration of the ME of GRB 211211A. Once the differential kinetic is exhausted or no longer supports another wind up of the toroidal magnetic field, the millisecond magnetar can continue to lose its rotation energy through magnetic dipole radiation. Furthermore, the model predicts that the different spikes of the burst are locally generated in small emission regions and are independent from one another, so the spectral lag will

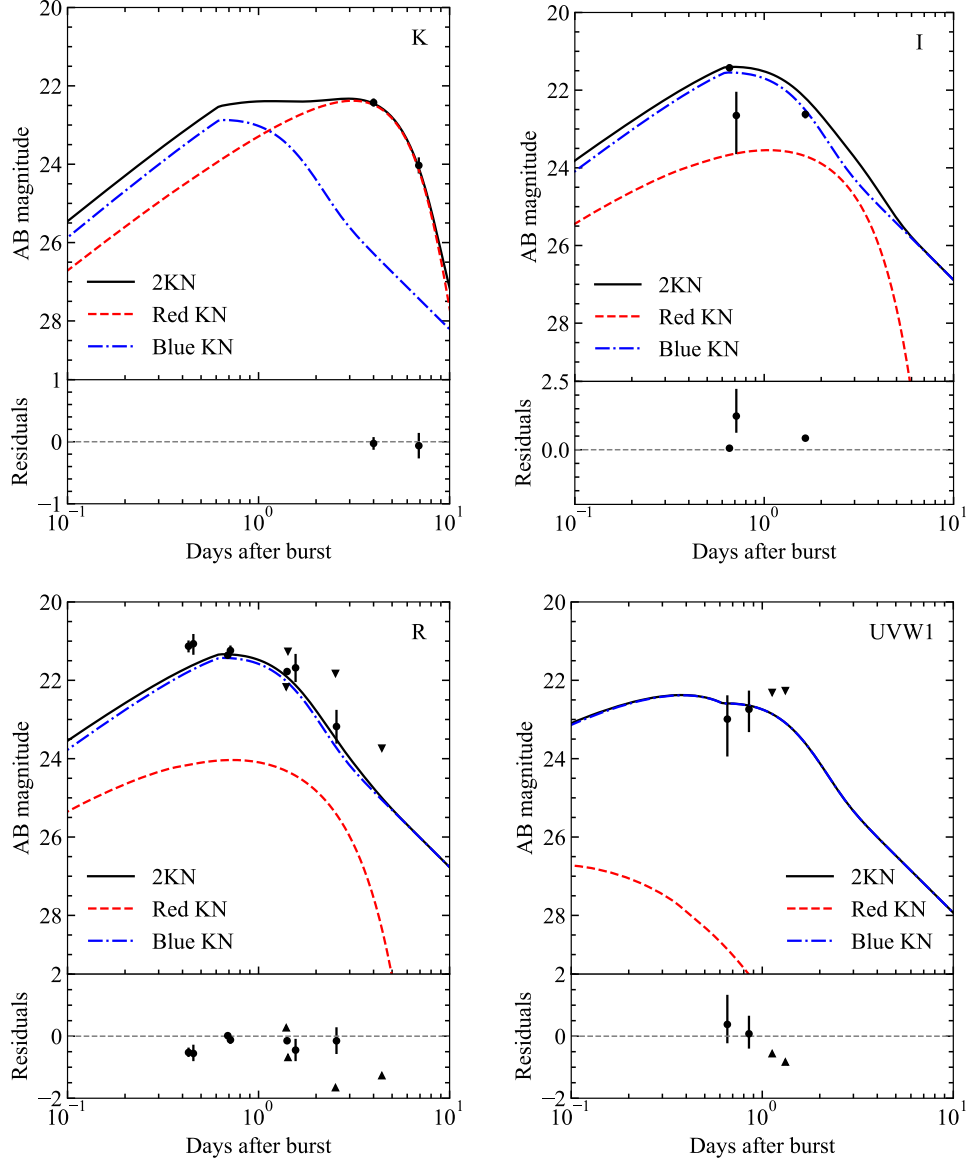


**Figure 11.** The AG-subtracted data (black circles), the two-component kilonova model (black line), and the individual KN components (red and blue lines) in four optical bands.

not exceed the timescale of the individual spikes. Such a prediction is in accordance with the observed tiny lags in GRB 211211A.

In comparison with the ME, the extended emission of GRB 211211A is systematically fainter in brightness, softer in spectra, smoother in variability, and locates on a different track in the Amati relation. These facts indicate that the physical origin of EE can differ from that of ME. One natural expectation is that, once the differential rotation power of the magnetic bubbles is no longer dominant, the magnetar’s spin-down power can serve as the primary energy source after the ME and continuously power up the burst for about  $\sim 55$  s.

The spin-down power of magnetar from magnetic dipole radiation has successfully explained the energy injection in the plateau phase (Zhang et al. 2006; Nousek et al. 2006). It has also been proposed to power the prompt emission GRBs (e.g., Usov 1992). Additionally, Lü et al. (2015) proposed that the extended emission detected in the *Swift*/BAT band is similar to the internal plateau emission in X-ray when the emission is bright and hard enough. The spin-down luminosity of a magnetar due to the magnetic dipole radiation can be calculated as (Shapiro et al. 1983; Zhang & Mészáros 2001b)

$$L_{\text{sd,m}} = \frac{B_{\text{rs}}^2 R_s^6 \Omega^4}{6c^3} \approx 10^{49} \text{ erg s}^{-1} B_{\text{rs},15}^2 R_{s,6}^6 P_{0,-3}^{-4}, \quad (7)$$

where  $B_{rs}$  represents the strength of poloidal magnetic field on the surface of the magnetar.  $R_s$  stands for the radius of the magnetar and  $c$  is the speed of light. It appears that in order to explain the observed luminosity of  $\sim 10^{49} - 10^{50} \text{ erg s}^{-1}$ , in the EE phase of GRB 211211A, a poloidal magnetic field  $B_{rs} \gtrsim 10^{15} \text{ G}$  is required, which is significantly stronger than the  $B_r$  value employed in the magnetic bubble model. Such an apparent inconsistency can be possibly alleviated by considering the following factors: (1) The poloidal magnetic field on the magnetar's surface may be different from that inside the magnetar. So  $B_{rs}$  is not necessarily to be identical to the value of  $B_r$  in the magnetic bubble case. In fact, some recent MHD-simulation on binary-neutron-star merges have shown that the amplification of magnetic field occurs in the shear layer between the two neutron stars, and in some cases,  $B_{rs}$  can be amplified to  $\gtrsim 10^{15} \text{ G}$ . However, low  $B$  regions, which remain as low as  $10^{13} \text{ G}$ , may still exist inside the magnetar before the amplified magnetic field is sufficiently advected with matter (Price & Rosswog 2006; Mösta et al. 2020; Palenzuela et al. 2021). (2) For different equation of state of magnetar, its radius and moment of inertia may undergo evolution when the magnetar spins down (Lan et al. 2021). If this is the case, the required  $B_{rs}$  can be decreased.

## 5. SUMMARY

In this Letter, We performed a comprehensive analysis of the multi-wavelength data of the nearby long-duration

GRB 211211A. The temporal and spectral characteristics of the burst, as well as the identification of a kilonova from long-term observations, all point to a merger-type origin. This burst is distinguished from other Type-I GRBs by its peculiarly long duration and spectrally hard extended emission. We suggest a feasible model that invokes a magnetar to release its energy through differential rotation-induced magnetic bubble radiation and magnetic dipole radiation, respectively, to drive the main and extended emission phases of the GRB. The model may also be applicable to previous similar events, such as GRB 060614. Additionally, our results confirm the the diversity of the type-I GRBs in terms of their duration and energy sources, as has long been proposed by Zhang et al. (2007a, 2009a). In addition, our results have reinforced the GRB classification method using multiple observational criteria (e.g., Zhang et al. 2009a; Li et al. 2016b, 2020) rather than relying solely on duration.

## ACKNOWLEDGEMENTS

We acknowledges support by the National Key Research and Development Programs of China (2018YFA0404204), the National Natural Science Foundation of China (Grant Nos. 11833003, U2038105, 12121003, 11922301), the science research grants from the China Manned Space Project with NO.CMS-CSST-2021-B11, and the Program for Innovative Talents, Entrepreneur in Jiangsu. We acknowledge the use of public data from the Fermi Science Support Center (FSSC).

## REFERENCES

- Abbott, B. P., Abbott, R., Abbott, T., et al. 2017, *Physical review letters*, 119, 161101
- Abbott, B. P., Abbott, R., Abbott, T. D., et al. 2017, *ApJL*, 848, L12, doi: [10.3847/2041-8213/aa91c9](https://doi.org/10.3847/2041-8213/aa91c9)
- Adelman-McCarthy, J. K., Agüeros, M. A., Allam, S. S., et al. 2008, *ApJS*, 175, 297, doi: [10.1086/524984](https://doi.org/10.1086/524984)
- Ahumada, T., Singer, L. P., Anand, S., et al. 2021, *Nature Astronomy*, 5, 917, doi: [10.1038/s41550-021-01428-7](https://doi.org/10.1038/s41550-021-01428-7)
- Amati, L., Della Valle, M., Frontera, F., et al. 2007, *A&A*, 463, 913, doi: [10.1051/0004-6361:20065994](https://doi.org/10.1051/0004-6361:20065994)
- Amati, L., Frontera, F., Tavani, M., et al. 2002, *A&A*, 390, 81, doi: [10.1051/0004-6361:20020722](https://doi.org/10.1051/0004-6361:20020722)
- Antonelli, L. A., D’Avanzo, P., Perna, R., et al. 2009, *A&A*, 507, L45, doi: [10.1051/0004-6361/200913062](https://doi.org/10.1051/0004-6361/200913062)
- Arcavi, I., Hosseinzadeh, G., Howell, D. A., et al. 2017, *Nature*, 551, 64, doi: [10.1038/nature24291](https://doi.org/10.1038/nature24291)
- Arnaud, K. A. 1996, in *Astronomical Society of the Pacific Conference Series*, Vol. 101, *Astronomical Data Analysis Software and Systems V*, ed. G. H. Jacoby & J. Barnes, 17
- Astropy Collaboration, Robitaille, T. P., Tollerud, E. J., et al. 2013, *A&A*, 558, A33, doi: [10.1051/0004-6361/201322068](https://doi.org/10.1051/0004-6361/201322068)
- Band, D., Matteson, J., Ford, L., et al. 1993, *ApJ*, 413, 281, doi: [10.1086/172995](https://doi.org/10.1086/172995)
- Barnes, J., & Kasen, D. 2013, *ApJ*, 775, 18, doi: [10.1088/0004-637X/775/1/18](https://doi.org/10.1088/0004-637X/775/1/18)
- Barthelmy, S. D., Barbier, L. M., Cummings, J. R., et al. 2005, *SSRv*, 120, 143, doi: [10.1007/s11214-005-5096-3](https://doi.org/10.1007/s11214-005-5096-3)
- Beardmore, A. P., Evans, P. A., Goad, M. R., Osborne, J. P., & Swift-XRT Team. 2021, *GRB Coordinates Network*, 31205, 1
- Beckwith, S. V. W., Stiavelli, M., Koekemoer, A. M., et al. 2006, *AJ*, 132, 1729, doi: [10.1086/507302](https://doi.org/10.1086/507302)

- Berger, E. 2010, *ApJ*, 722, 1946, doi: [10.1088/0004-637X/722/2/1946](https://doi.org/10.1088/0004-637X/722/2/1946)
- . 2014, *ARA&A*, 52, 43, doi: [10.1146/annurev-astro-081913-035926](https://doi.org/10.1146/annurev-astro-081913-035926)
- Berger, E., Fong, W., & Chornock, R. 2013, *ApJL*, 774, L23, doi: [10.1088/2041-8205/774/2/L23](https://doi.org/10.1088/2041-8205/774/2/L23)
- Berlato, F., Greiner, J., & Burgess, J. M. 2019, *ApJ*, 873, 60, doi: [10.3847/1538-4357/ab0413](https://doi.org/10.3847/1538-4357/ab0413)
- Bernardini, M. G., Ghirlanda, G., Campana, S., et al. 2015, *MNRAS*, 446, 1129, doi: [10.1093/mnras/stu2153](https://doi.org/10.1093/mnras/stu2153)
- Blanchard, P. K., Berger, E., & Fong, W.-f. 2016, *ApJ*, 817, 144, doi: [10.3847/0004-637X/817/2/144](https://doi.org/10.3847/0004-637X/817/2/144)
- Bloom, J. S., Kulkarni, S. R., & Djorgovski, S. G. 2002, *AJ*, 123, 1111, doi: [10.1086/338893](https://doi.org/10.1086/338893)
- Buchner, J., Georgakakis, A., Nandra, K., et al. 2014, *A&A*, 564, A125, doi: [10.1051/0004-6361/201322971](https://doi.org/10.1051/0004-6361/201322971)
- Burgess, J. M., Yu, H.-F., Greiner, J., & Mortlock, D. J. 2018, *MNRAS*, 476, 1427, doi: [10.1093/mnras/stx2853](https://doi.org/10.1093/mnras/stx2853)
- Burrows, D. N., Hill, J. E., Nousek, J. A., et al. 2005, *SSRv*, 120, 165, doi: [10.1007/s11214-005-5097-2](https://doi.org/10.1007/s11214-005-5097-2)
- Cano, Z. 2013, *MNRAS*, 434, 1098, doi: [10.1093/mnras/stt1048](https://doi.org/10.1093/mnras/stt1048)
- Chornock, R., Berger, E., Kasen, D., et al. 2017, *ApJL*, 848, L19, doi: [10.3847/2041-8213/aa905c](https://doi.org/10.3847/2041-8213/aa905c)
- Clocchiatti, A., Suntzeff, N. B., Covarrubias, R., & Candia, P. 2011, *AJ*, 141, 163, doi: [10.1088/0004-6256/141/5/163](https://doi.org/10.1088/0004-6256/141/5/163)
- Coulter, D., Foley, R., Kilpatrick, C., et al. 2017, *Science*, 358, 1556
- Cowperthwaite, P. S., Berger, E., Villar, V. A., et al. 2017, *ApJL*, 848, L17, doi: [10.3847/2041-8213/aa8fc7](https://doi.org/10.3847/2041-8213/aa8fc7)
- D’Ai, A., Ambrosi, E., D’Elia, V., et al. 2021, *GRB Coordinates Network*, 31202, 1
- Dai, Z. G., & Lu, T. 1998, *PhRvL*, 81, 4301, doi: [10.1103/PhysRevLett.81.4301](https://doi.org/10.1103/PhysRevLett.81.4301)
- Dai, Z. G., Wang, X. Y., Wu, X. F., & Zhang, B. 2006, *Science*, 311, 1127, doi: [10.1126/science.1123606](https://doi.org/10.1126/science.1123606)
- Della Valle, M., Chincarini, G., Panagia, N., et al. 2006, *Nature*, 444, 1050, doi: [10.1038/nature05374](https://doi.org/10.1038/nature05374)
- Deng, W., & Zhang, B. 2014, *ApJ*, 785, 112, doi: [10.1088/0004-637X/785/2/112](https://doi.org/10.1088/0004-637X/785/2/112)
- Dermer, C. D. 2004, *ApJ*, 614, 284, doi: [10.1086/426532](https://doi.org/10.1086/426532)
- Dessart, L., Ott, C. D., Burrows, A., Rosswog, S., & Livne, E. 2008, *The Astrophysical Journal*, 690, 1681, doi: [10.1088/0004-637x/690/2/1681](https://doi.org/10.1088/0004-637x/690/2/1681)
- Drout, M. R., Piro, A. L., Shappee, B. J., et al. 2017, *Science*, 358, 1570, doi: [10.1126/science.aag0049](https://doi.org/10.1126/science.aag0049)
- Evans, P. A., Cenko, S. B., Kennea, J. A., et al. 2017, *Science*, 358, 1565, doi: [10.1126/science.aap9580](https://doi.org/10.1126/science.aap9580)
- Fan, Y.-Z., Yu, Y.-W., Xu, D., et al. 2013, *ApJL*, 779, L25, doi: [10.1088/2041-8205/779/2/L25](https://doi.org/10.1088/2041-8205/779/2/L25)
- Fermi GBM Team. 2021, *GRB Coordinates Network*, 31201, 1
- Fermi-LAT Collaboration, Ajello, M., Atwood, W. B., et al. 2021, *Nature Astronomy*, 5, 385, doi: [10.1038/s41550-020-01287-8](https://doi.org/10.1038/s41550-020-01287-8)
- Feroz, F., & Hobson, M. P. 2008, *MNRAS*, 384, 449, doi: [10.1111/j.1365-2966.2007.12353.x](https://doi.org/10.1111/j.1365-2966.2007.12353.x)
- Feroz, F., Hobson, M. P., & Bridges, M. 2009, *MNRAS*, 398, 1601, doi: [10.1111/j.1365-2966.2009.14548.x](https://doi.org/10.1111/j.1365-2966.2009.14548.x)
- Feroz, F., Hobson, M. P., Cameron, E., & Pettitt, A. N. 2019, *The Open Journal of Astrophysics*, 2, 10, doi: [10.21105/astro.1306.2144](https://doi.org/10.21105/astro.1306.2144)
- Fitzpatrick, E. L. 1999, *PASP*, 111, 63, doi: [10.1086/316293](https://doi.org/10.1086/316293)
- Fong, W., & Berger, E. 2013, *ApJ*, 776, 18, doi: [10.1088/0004-637X/776/1/18](https://doi.org/10.1088/0004-637X/776/1/18)
- Foreman-Mackey, D., Hogg, D. W., Lang, D., & Goodman, J. 2013, *PASP*, 125, 306, doi: [10.1086/670067](https://doi.org/10.1086/670067)
- Fynbo, J. P. U., Watson, D., Thöne, C. C., et al. 2006, *Nature*, 444, 1047, doi: [10.1038/nature05375](https://doi.org/10.1038/nature05375)
- Gal-Yam, A., Fox, D. B., Price, P. A., et al. 2006, *Nature*, 444, 1053, doi: [10.1038/nature05373](https://doi.org/10.1038/nature05373)
- Galama, T. J., Vreeswijk, P. M., van Paradijs, J., et al. 1998, *Nature*, 395, 670, doi: [10.1038/27150](https://doi.org/10.1038/27150)
- Gao, H., Cao, Z., Ai, S., & Zhang, B. 2017, *ApJL*, 851, L45, doi: [10.3847/2041-8213/aaa0c6](https://doi.org/10.3847/2041-8213/aaa0c6)
- Gehrels, N., Chincarini, G., Giommi, P., et al. 2004, *ApJ*, 611, 1005, doi: [10.1086/422091](https://doi.org/10.1086/422091)
- Gehrels, N., Norris, J. P., Barthelmy, S. D., et al. 2006, *Nature*, 444, 1044, doi: [10.1038/nature05376](https://doi.org/10.1038/nature05376)
- Goldstein, A., Veres, P., Burns, E., et al. 2017, *The Astrophysical Journal Letters*, 848, L14
- Golenetskii, S., Aptekar, R., Mazets, E., et al. 2006, *GRB Coordinates Network*, 5264, 1
- Guillochon, J., Nicholl, M., Villar, V. A., et al. 2018, *ApJS*, 236, 6, doi: [10.3847/1538-4365/aab761](https://doi.org/10.3847/1538-4365/aab761)
- Hjorth, J., Sollerman, J., Møller, P., et al. 2003, *Nature*, 423, 847, doi: [10.1038/nature01750](https://doi.org/10.1038/nature01750)
- Hogg, D. W., Pahre, M. A., McCarthy, J. K., et al. 1997, *MNRAS*, 288, 404, doi: [10.1093/mnras/288.2.404](https://doi.org/10.1093/mnras/288.2.404)
- Hotokezaka, K., Kiuchi, K., Kyutoku, K., et al. 2013, *Phys. Rev. D*, 87, 024001, doi: [10.1103/PhysRevD.87.024001](https://doi.org/10.1103/PhysRevD.87.024001)
- Kann, D. A., Klose, S., Zhang, B., et al. 2011, *ApJ*, 734, 96, doi: [10.1088/0004-637X/734/2/96](https://doi.org/10.1088/0004-637X/734/2/96)
- Kasen, D., Badnell, N. R., & Barnes, J. 2013, *ApJ*, 774, 25, doi: [10.1088/0004-637X/774/1/25](https://doi.org/10.1088/0004-637X/774/1/25)
- Kasen, D., Metzger, B., Barnes, J., Quataert, E., & Ramirez-Ruiz, E. 2017, *Nature*, 551, 80, doi: [10.1038/nature24453](https://doi.org/10.1038/nature24453)
- Kilpatrick, C. D., Foley, R. J., Kasen, D., et al. 2017, *Science*, 358, 1583, doi: [10.1126/science.aag0073](https://doi.org/10.1126/science.aag0073)

- Kluźniak, W., & Ruderman, M. 1998, *ApJL*, 505, L113, doi: [10.1086/311622](https://doi.org/10.1086/311622)
- Kumar, P., & Panaitescu, A. 2000, *ApJL*, 541, L51, doi: [10.1086/312905](https://doi.org/10.1086/312905)
- Kyutoku, K., Ioka, K., & Shibata, M. 2013, *Phys. Rev. D*, 88, 041503, doi: [10.1103/PhysRevD.88.041503](https://doi.org/10.1103/PhysRevD.88.041503)
- Lan, L., Gao, H., Ai, S., & Li, S.-Z. 2021, *ApJ*, 919, 14, doi: [10.3847/1538-4357/ac167d](https://doi.org/10.3847/1538-4357/ac167d)
- Lattimer, J. M., & Schramm, D. N. 1974, *ApJL*, 192, L145, doi: [10.1086/181612](https://doi.org/10.1086/181612)
- Levesque, E. M., Bloom, J. S., Butler, N. R., et al. 2010, *MNRAS*, 401, 963, doi: [10.1111/j.1365-2966.2009.15733.x](https://doi.org/10.1111/j.1365-2966.2009.15733.x)
- Li, L., Geng, J.-J., Meng, Y.-Z., et al. 2019, *ApJ*, 884, 109, doi: [10.3847/1538-4357/ab40b9](https://doi.org/10.3847/1538-4357/ab40b9)
- Li, L.-X., & Paczyński, B. 1998, *ApJL*, 507, L59, doi: [10.1086/311680](https://doi.org/10.1086/311680)
- Li, Y., Zhang, B., & Lü, H.-J. 2016a, *ApJS*, 227, 7, doi: [10.3847/0067-0049/227/1/7](https://doi.org/10.3847/0067-0049/227/1/7)
- . 2016b, *ApJS*, 227, 7, doi: [10.3847/0067-0049/227/1/7](https://doi.org/10.3847/0067-0049/227/1/7)
- Li, Y., Zhang, B., & Yuan, Q. 2020, *ApJ*, 897, 154, doi: [10.3847/1538-4357/ab96b8](https://doi.org/10.3847/1538-4357/ab96b8)
- Lien, A., Sakamoto, T., Barthelmy, S. D., et al. 2016, *ApJ*, 829, 7, doi: [10.3847/0004-637X/829/1/7](https://doi.org/10.3847/0004-637X/829/1/7)
- Lü, H.-J., Zhang, B., Lei, W.-H., Li, Y., & Lasky, P. D. 2015, *ApJ*, 805, 89, doi: [10.1088/0004-637X/805/2/89](https://doi.org/10.1088/0004-637X/805/2/89)
- Lü, H.-J., Zhang, B., Liang, E.-W., Zhang, B.-B., & Sakamoto, T. 2014, *MNRAS*, 442, 1922, doi: [10.1093/mnras/stu982](https://doi.org/10.1093/mnras/stu982)
- Lü, H.-J., Yuan, H.-Y., Yi, T.-F., et al. 2022, arXiv e-prints, arXiv:2201.06395. <https://arxiv.org/abs/2201.06395>
- Lu, R.-J., Wei, J.-J., Liang, E.-W., et al. 2012, *ApJ*, 756, 112, doi: [10.1088/0004-637X/756/2/112](https://doi.org/10.1088/0004-637X/756/2/112)
- Lyons, N., O'Brien, P. T., Zhang, B., et al. 2010, *MNRAS*, 402, 705, doi: [10.1111/j.1365-2966.2009.15538.x](https://doi.org/10.1111/j.1365-2966.2009.15538.x)
- Malesani, D. B., Fynbo, J. P. U., de Ugarte Postigo, A., et al. 2021, *GRB Coordinates Network*, 31221, 1
- Meegan, C., Lichti, G., Bhat, P. N., et al. 2009, *ApJ*, 702, 791, doi: [10.1088/0004-637X/702/1/791](https://doi.org/10.1088/0004-637X/702/1/791)
- Mészáros, P., & Rees, M. J. 2000, *ApJ*, 530, 292, doi: [10.1086/308371](https://doi.org/10.1086/308371)
- Metzger, B. D., & Fernández, R. 2014, *MNRAS*, 441, 3444, doi: [10.1093/mnras/stu802](https://doi.org/10.1093/mnras/stu802)
- Metzger, B. D., Martínez-Pinedo, G., Darbha, S., et al. 2010, *MNRAS*, 406, 2650, doi: [10.1111/j.1365-2966.2010.16864.x](https://doi.org/10.1111/j.1365-2966.2010.16864.x)
- Mösta, P., Radice, D., Haas, R., Schnetter, E., & Bernuzzi, S. 2020, *ApJL*, 901, L37, doi: [10.3847/2041-8213/abb6ef](https://doi.org/10.3847/2041-8213/abb6ef)
- Narayana Bhat, P., Meegan, C. A., von Kienlin, A., et al. 2016, *ApJS*, 223, 28, doi: [10.3847/0067-0049/223/2/28](https://doi.org/10.3847/0067-0049/223/2/28)
- Nicholl, M., Berger, E., Kasen, D., et al. 2017, *ApJL*, 848, L18, doi: [10.3847/2041-8213/aa9029](https://doi.org/10.3847/2041-8213/aa9029)
- Norris, J. P., Marani, G. F., & Bonnell, J. T. 2000, *ApJ*, 534, 248, doi: [10.1086/308725](https://doi.org/10.1086/308725)
- Nousek, J. A., Kouveliotou, C., Grupe, D., et al. 2006, *ApJ*, 642, 389, doi: [10.1086/500724](https://doi.org/10.1086/500724)
- Palenzuela, C., Aguilera-Miret, R., Carrasco, F., et al. 2021, arXiv e-prints, arXiv:2112.08413. <https://arxiv.org/abs/2112.08413>
- Pian, E., D'Avanzo, P., Benetti, S., et al. 2017, *Nature*, 551, 67, doi: [10.1038/nature24298](https://doi.org/10.1038/nature24298)
- Preece, R. D., Briggs, M. S., Mallozzi, R. S., et al. 1998, *ApJL*, 506, L23, doi: [10.1086/311644](https://doi.org/10.1086/311644)
- Price, D. J., & Rosswog, S. 2006, *Science*, 312, 719, doi: [10.1126/science.1125201](https://doi.org/10.1126/science.1125201)
- Racusin, J. L., Liang, E. W., Burrows, D. N., et al. 2009, *ApJ*, 698, 43, doi: [10.1088/0004-637X/698/1/43](https://doi.org/10.1088/0004-637X/698/1/43)
- Rees, M. J., & Mészáros, P. 1998, *ApJL*, 496, L1, doi: [10.1086/311244](https://doi.org/10.1086/311244)
- Reeves, J. N., Watson, D., Osborne, J. P., et al. 2002, *Nature*, 416, 512, doi: [10.1038/416512a](https://doi.org/10.1038/416512a)
- Roberts, O. J., Veres, P., Baring, M. G., et al. 2021, *Nature*, 589, 207, doi: [10.1038/s41586-020-03077-8](https://doi.org/10.1038/s41586-020-03077-8)
- Roming, P. W. A., Kennedy, T. E., Mason, K. O., et al. 2005, *SSRv*, 120, 95, doi: [10.1007/s11214-005-5095-4](https://doi.org/10.1007/s11214-005-5095-4)
- Rosswog, S. 2005, *ApJ*, 634, 1202, doi: [10.1086/497062](https://doi.org/10.1086/497062)
- Rosswog, S., Liebendörfer, M., Thielemann, F. K., et al. 1999, *A&A*, 341, 499. <https://arxiv.org/abs/astro-ph/9811367>
- Ruderman, M. A., Tao, L., & Kluźniak, W. 2000, *ApJ*, 542, 243, doi: [10.1086/309537](https://doi.org/10.1086/309537)
- Ryan, G., van Eerten, H., Piro, L., & Troja, E. 2020, *ApJ*, 896, 166, doi: [10.3847/1538-4357/ab93cf](https://doi.org/10.3847/1538-4357/ab93cf)
- Sari, R., & Mészáros, P. 2000, *ApJL*, 535, L33, doi: [10.1086/312689](https://doi.org/10.1086/312689)
- Scargle, J. D., Norris, J. P., Jackson, B., & Chiang, J. 2013, *ApJ*, 764, 167, doi: [10.1088/0004-637X/764/2/167](https://doi.org/10.1088/0004-637X/764/2/167)
- Schwarz, G. 1978, *Annals of Statistics*, 6, 461
- Shao, L., Zhang, B.-B., Wang, F.-R., et al. 2017, *ApJ*, 844, 126, doi: [10.3847/1538-4357/aa7d01](https://doi.org/10.3847/1538-4357/aa7d01)
- Shapiro, S. L., Teukolsky, S. A., & Lightman, A. P. 1983, *Physics Today*, 36, 89, doi: [10.1063/1.2915325](https://doi.org/10.1063/1.2915325)
- Shappee, B. J., Simon, J. D., Drout, M. R., et al. 2017, *Science*, 358, 1574, doi: [10.1126/science.aag0186](https://doi.org/10.1126/science.aag0186)
- Smartt, S. J., Chen, T. W., Jerkstrand, A., et al. 2017, *Nature*, 551, 75, doi: [10.1038/nature24303](https://doi.org/10.1038/nature24303)
- Stalder, B., Tonry, J., Smartt, S. J., et al. 2017, *ApJ*, 850, 149, doi: [10.3847/1538-4357/aa95c1](https://doi.org/10.3847/1538-4357/aa95c1)
- Svinkin, D., Frederiks, D., Hurley, K., et al. 2021, *Nature*, 589, 211, doi: [10.1038/s41586-020-03076-9](https://doi.org/10.1038/s41586-020-03076-9)

- Tanvir, N. R., Levan, A. J., Fruchter, A. S., et al. 2013, *Nature*, 500, 547, doi: [10.1038/nature12505](https://doi.org/10.1038/nature12505)
- Tanvir, N. R., Levan, A. J., González-Fernández, C., et al. 2017, *ApJL*, 848, L27, doi: [10.3847/2041-8213/aa90b6](https://doi.org/10.3847/2041-8213/aa90b6)
- Troja, E., Cusumano, G., O’Brien, P. T., et al. 2007, *ApJ*, 665, 599, doi: [10.1086/519450](https://doi.org/10.1086/519450)
- Uhm, Z. L., & Zhang, B. 2014, *Nature Physics*, 10, 351, doi: [10.1038/nphys2932](https://doi.org/10.1038/nphys2932)
- Ukwatta, T. N., Stamatikos, M., Dhuga, K. S., et al. 2010, *ApJ*, 711, 1073, doi: [10.1088/0004-637X/711/2/1073](https://doi.org/10.1088/0004-637X/711/2/1073)
- Usov, V. V. 1992, *Nature*, 357, 472, doi: [10.1038/357472a0](https://doi.org/10.1038/357472a0)
- Vianello, G., Gill, R., Granot, J., et al. 2018, *ApJ*, 864, 163, doi: [10.3847/1538-4357/aad6ea](https://doi.org/10.3847/1538-4357/aad6ea)
- Villar, V. A., Guillochon, J., Berger, E., et al. 2017, *ApJL*, 851, L21, doi: [10.3847/2041-8213/aa9c84](https://doi.org/10.3847/2041-8213/aa9c84)
- von Kienlin, A., Meegan, C. A., Paciesas, W. S., et al. 2020, *ApJ*, 893, 46, doi: [10.3847/1538-4357/ab7a18](https://doi.org/10.3847/1538-4357/ab7a18)
- Wang, X.-G., Zhang, B., Liang, E.-W., et al. 2015, *ApJS*, 219, 9, doi: [10.1088/0067-0049/219/1/9](https://doi.org/10.1088/0067-0049/219/1/9)
- Xin, L.-P., Liang, E.-W., Wei, J.-Y., et al. 2011, *MNRAS*, 410, 27, doi: [10.1111/j.1365-2966.2010.17419.x](https://doi.org/10.1111/j.1365-2966.2010.17419.x)
- Yang, B., Jin, Z.-P., Li, X., et al. 2015, *Nature Communications*, 6, 7323, doi: [10.1038/ncomms8323](https://doi.org/10.1038/ncomms8323)
- Yang, J., Chand, V., Zhang, B.-B., et al. 2020, *ApJ*, 899, 106, doi: [10.3847/1538-4357/aba745](https://doi.org/10.3847/1538-4357/aba745)
- Yi, T., Liang, E., Qin, Y., & Lu, R. 2006, *MNRAS*, 367, 1751, doi: [10.1111/j.1365-2966.2006.10083.x](https://doi.org/10.1111/j.1365-2966.2006.10083.x)
- Zhang, B., Fan, Y. Z., Dyks, J., et al. 2006, *ApJ*, 642, 354, doi: [10.1086/500723](https://doi.org/10.1086/500723)
- Zhang, B., & Mészáros, P. 2001a, *ApJL*, 552, L35, doi: [10.1086/320255](https://doi.org/10.1086/320255)
- . 2001b, *ApJL*, 552, L35, doi: [10.1086/320255](https://doi.org/10.1086/320255)
- . 2002, *ApJ*, 581, 1236, doi: [10.1086/344338](https://doi.org/10.1086/344338)
- Zhang, B., & Yan, H. 2011, *ApJ*, 726, 90, doi: [10.1088/0004-637X/726/2/90](https://doi.org/10.1088/0004-637X/726/2/90)
- Zhang, B., Zhang, B.-B., Liang, E.-W., et al. 2007a, *ApJL*, 655, L25, doi: [10.1086/511781](https://doi.org/10.1086/511781)
- Zhang, B., Zhang, B.-B., Virgili, F. J., et al. 2009a, *ApJ*, 703, 1696, doi: [10.1088/0004-637X/703/2/1696](https://doi.org/10.1088/0004-637X/703/2/1696)
- Zhang, B.-B., Liang, E.-W., & Zhang, B. 2007b, *ApJ*, 666, 1002, doi: [10.1086/519548](https://doi.org/10.1086/519548)
- Zhang, B.-B., Zhang, B., Liang, E.-W., & Wang, X.-Y. 2009b, *ApJL*, 690, L10, doi: [10.1088/0004-637X/690/1/L10](https://doi.org/10.1088/0004-637X/690/1/L10)
- Zhang, B.-B., Burrows, D. N., Zhang, B., et al. 2012, *ApJ*, 748, 132, doi: [10.1088/0004-637X/748/2/132](https://doi.org/10.1088/0004-637X/748/2/132)
- Zhang, B.-B., Zhang, B., Sun, H., et al. 2018, *Nature communications*, 9, 1
- Zhang, B. B., Zhang, B., Castro-Tirado, A. J., et al. 2018, *Nature Astronomy*, 2, 69, doi: [10.1038/s41550-017-0309-8](https://doi.org/10.1038/s41550-017-0309-8)
- Zhang, B. B., Liu, Z. K., Peng, Z. K., et al. 2021, *Nature Astronomy*, 5, 911, doi: [10.1038/s41550-021-01395-z](https://doi.org/10.1038/s41550-021-01395-z)
- Zhang, H.-M., Liu, R.-Y., Zhong, S.-Q., & Wang, X.-Y. 2020, *ApJL*, 903, L32, doi: [10.3847/2041-8213/abc2c9](https://doi.org/10.3847/2041-8213/abc2c9)
- Zheng, W., Filippenko, A. V., & KAIT GRB Team. 2021, *GRB Coordinates Network*, 31203, 1